International Journal of Mechanical Sciences 263 (2024) 108779



Contents lists available at ScienceDirect

## International Journal of Mechanical Sciences

journal homepage: www.elsevier.com/locate/ijmecsci



## Modelling of a general lumped-compliance beam for compliant mechanisms



Jiaxiang Zhu, Guangbo Hao

School of Engineering and Architecture-Electrical and Electronic Engineering, University College Cork, Cork, Ireland

ARTICLE INFO

Keywords:
Compliant mechanisms
General lumped-compliance beam
Nonlinear kinetostatic modeling
Beam constraint model

#### ABSTRACT

Compliant mechanisms are crucial in a wide range of applications, and straight flexure beams with uniform thickness serve as their fundamental building blocks. While techniques and methods exist to estimate the sophisticated load-displacement behavior of these beams, dealing with the nonlinear large deformation and parametric design of complex compliant mechanisms using these beams remains a significant challenge. To address this challenge, an analytical model has been developed to integrate six independent geometric parameters into a general lumped-compliance beam, known as the general lumped-compliance beam model (GLBM). This approach enables the determinate synthesis of force-displacement characteristics in compliant mechanisms that feature any two flexure beams connected in series, such as the conventional lumped-compliance beam, distributed beam, inverted beam, and folded beam. The closed-form beam constraint model (BCM) is utilized to derive the GLBM that accurately captures geometric nonlinearity and load-dependent effects. To demonstrate the effectiveness of this modeling technique, we verified five specific configurations of the GLBM using nonlinear finite element analysis (FEA). In addition, we selected two representative compliant mechanisms, a revolute joint and a bistable mechanism, for nonlinear analysis and experimental validation, which further showcases the efficacy of this proposed GLBM.

### 1. Introduction

Over the past few decades, compliant mechanisms have gained widespread recognition due to their merits such as no backlash, wearfree, and low noise [1]. They have opened up new horizons in nanopositioning development [2-4], energy harvesting [5-7], microelectromechanical systems (MEMS) [8–10], etc. Compliant mechanisms often present a monolithic body with either lumped-compliance beams or distributed-compliance beams, which exhibit different deformation characteristics. The lumped-compliance beam, usually combining two elastic notch-type hinges and a rigid-body link, has a limited deformarange [11]. However, the deformation distributed-compliance beam occurs along the whole beam and is, therefore, much larger [12]. Both types of beams are widely used in the design of compliant building blocks including bistable mechanism [13-15], statistically-balanced mechanism [16], compliant amplifier [17,18], translational joint [19,20], rotational joint [21,22]. Therefore, it is the intention of this paper to come up with a model that is simple, accurate, and applicable to a more general lumped-compliance beam for large deflections, which can facilitate the parametric design of compliant mechanisms. Here, a general lumped-compliance beam has more design parameters than a conventional lumped-compliance beam, which is inspired by the position space concept [22]. The general lumped-compliance beams can find their specific applications in the design of bistable mechanisms with equal switch forces [14], compliant tensural multi-stable mechanisms [23], and a novel parallelogram mechanism [24].

The finite element analysis (FEA) method is a popular and effective numerical approach for analyzing the kinetostatics and dynamics of compliant mechanisms, thanks to its ability to handle complex geometries and boundary conditions. However, there are some inherent drawbacks associated with this method. While users have complete control over model manipulation, they cannot guarantee its accuracy. Additionally, discretization errors and stress singularities can cause unconverged solutions, particularly when compressive forces are applied to flexure beams. Consequently, the FEA method may produce incorrect or unrealistic shape configurations. In general, the accuracy of the FEA method depends on various factors, including the degrees of freedom, discretization, and element type used [25].

Apart from the FEA method, a considerable number of modeling methods have been developed for kinetostatic or dynamic modeling of compliant mechanisms. These methods include the pseudo-rigid-body

E-mail address: G.Hao@ucc.ie (G. Hao).

<sup>\*</sup> Corresponding author.

model (PRBM), beam constraint model (BCM) [20], smooth curvature model (SCM) [26], elliptic integral solution (EIS) and their derivatives like chained-BCM (CBCM) [27], Timoshenko-BCM (TBCM) [28], the integral method based BCM (IMBCM) [29,30], spatial-BCM (SBCM) [31, 32], chained-PRBM (CPRBM) [33–35], PRBM-based dynamic model [36], comprehensive-EIS (CEIS) [37], multiple-SCM (MSCM) [38].

The PRBM generally serves as an effective modeling method in the early-stage design of compliant mechanisms, where the nonlinear deflection of a flexure beam is approximated as a series of torsional springs or linear springs connected by rigid mechanisms [39,40]. As a result of the limited degree of freedom, the 1R-PRBM has load dependent effect degrading the accuracy of the model. To improve the accuracy of 1R-PRBM, the 2R-PRBM [34], 3R-PRBM [35,41], 5R-PRBM [42], and CPRBM [43,44] were prosed. However, a higher amount of discretization of the PRBM model inevitably leads to higher dimensional mathematical models, which causes longer computational time. They are not capable of capturing the elasto-kinematic effect and large errors in response to arbitrary loads, which is another significant hinder in the application of compliant mechanism synthesize.

The BCM is based on the Euler-Bernoulli beam model and considers geometric nonlinearity and load-dependent effect associated with linearized beam curvature assumptions. It is simple, parametric, closedform, and accurately predicts the behavior of flexure beams with intermediate deflections [45]. As aforementioned, BCM has been extended for different modeling scenarios of nonlinear deflections, including the SBCM [46,47], CBCM [27], IMBCM [29,30], TBCM [28], BCM with semi-rigid element [48]. The SBCM is capable of capturing the spatial motion of a wire beam. The CBCM discretizes a flexure beam into multiple segments to extend the range of the allowable axial load and the deflection. The CBCM with only two BCM elements, commonly known as Bi-BCM, is widely preferred and adopted due to its balance between accuracy and simplicity [49,50]. The IMBCM is proposed to model nonlinear fillet leaf springs. The TBCM incorporates the sheer effect which can model stubby beams. The BCM with a semi-rigid element is a method based on BCM to investigate the nonlinear static load-displacement relationships of beam-based flexure modules containing an intermediate semi-rigid element. An intermediate stiffening element is commonly treated as a perfect rigid element. The BCM with a semi-rigid element removes this untrue assumption, which is more accurate. The BCM modeling method is a versatile and easy-to-use tool that can be integrated into various modeling scenarios.

A classic method for solving large deflections (more than 0.15 of the beam's length) of a compliant mechanism is the EIS, which is an exact solution to the Euler-Bernoulli beam equation. However, it is limited to the range of slope angles and has no inflection point [51–53]. To overcome the limitations of no inflection point, an EIS for a large beam deflection with an inflection point subject to arbitrary loading conditions was derived in reference [54]. In [37], a CEIS with multiple inflection points and subject to arbitrary loading was proposed. To eliminate the limitation of the range of slope angles, an alternative method was introduced in [52]. The original EIS has been improved in terms of the inflection point, end loads, and slope angles. However, it is not a preferred technique for intermediate displacement ranges due to its rather complex derivation and implementation. For instance, the derivation process may be sensitive to initial guesses of unknown parameters if the end slope and load parameters are not provided [55].

As opposed to many other modeling techniques that involve numerical integration or discretization, the SCM [26] assumes that the curvature of a beam in bending is smooth and can therefore be approximated by low-order polynomials (e.g., Legendre polynomials). This approach enables the extraction of kinematic Jacobians and

Hessians, as well as generalized stiffness matrices, which can be used to predict the deformation or stiffness of structures with multiple links. Additionally, it is capable of predicting the first several buckling modes, making it an attractive method for designing graspers [56–58]. However, this approach is not suitable to synthesize planar-compliant mechanisms such as those for finger-type robots. Additionally, synthesizing more complex mechanisms using the smooth curvature mode has not been thoroughly studied.

As previously discussed, these models have certain limitations, such as their inability to accurately predict large deflection and inflection points, and/or their large difficulty in being applied to complex structures. Therefore, this study aims to address these problems by incorporating more geometric parameters into a lumped-compliance beam and proposing a general lumped-compliance beam model (GLBM). Outlined below are the primary benefits of utilizing the GLBM:

- Simply by regulating the six geometry parameters, the GLBM can
  effectively predict the force-displacement characteristics of a general
  lumped-compliance beam that features any two flexure beams connected in series and with a rigid body between them. The model can
  deal with all special design cases such as the folded beam and
  inverted lumped-compliance beam.
- 2) The developed GLBM has increased accuracy while predicting the large-deformation kinetostatic characteristic. Notably, the GLBM extends the application range of allowable axial forces. For instance, it increases the allowable normalized compressive axial force from  $\pi^2 EI/(4L^2)$  to  $\pi^2 EI/L^2$ , if a straight distributed-compliance flexure beam is divided into two equal segments [59,55]. Another strength of this model is its ability to accurately predict the load-displacement relations and deformation in certain designs, such as a bistable mechanism, with two inflection points along the deformed beam,

#### 2. General lumped-compliance beam model

The objective of this section is to introduce the derivation of the GLBM. The section begins by presenting the BCM as a basis for the development of the model, which is documented in Appendix A. Subsequently, the derivation of the GLBM is elaborated step by step, providing detailed explanations of the process.

Fig. 1(a) shows the parameterized lumped-compliance beam that features two flexure beams connected in serial. The GLBM is dominantly defined by six geometrical parameters, i.e.,  $L_{i1}$ ,  $L_{i2}$ ,  $\gamma_b$   $\alpha_b$   $\beta_i$ , and  $W_{ib}$  which are labeled in Fig. 1(a). The symbol i corresponds to a general beam configuration. It is worth noting that the length W is the distance between the two center points (labeled as  $C_{p1}$  and  $C_{p2}$ ) of the two flexure beams. By manipulating these parameters, we can obtain any beam configurations that consist of any two flexure beams and one rigid stage in the middle (including only two flexure beams without a rigid stage as defined below).

$$W_i \cos(\gamma) = L_{i1} \cos(\alpha_i)/2 + L_{i2} \cos(\beta_i)/2 \text{ and } W_i \sin(\gamma_i) = L_{i1} \sin(\alpha_i)/2$$
  
+  $L_{i2} \sin(\beta_i)/2$  (1)

To obtain the relationship between the tip input forces  $(F_{\rm Sib}\ P_{\rm Sib}\ M_{\rm Si})$  and the tip output displacements  $(X_{\rm Sib}\ Y_{\rm Sib}\ \theta_{\rm Si})$  with respect to the coordinate frame X-Y-Z, we utilize the BCM in conjunction with the Free Body Diagram (FBD) method. This approach is what we commonly used in solving a typical mechanic problem which involves three components: constitutive equations, force equilibrium, and geometry compatibility [60–62]. The constitutive equation of each flexure beam is obtained from the BCM [45], which is explained in Appendix A.

The constitutive equations of flexure beam 1 can be expressed below.

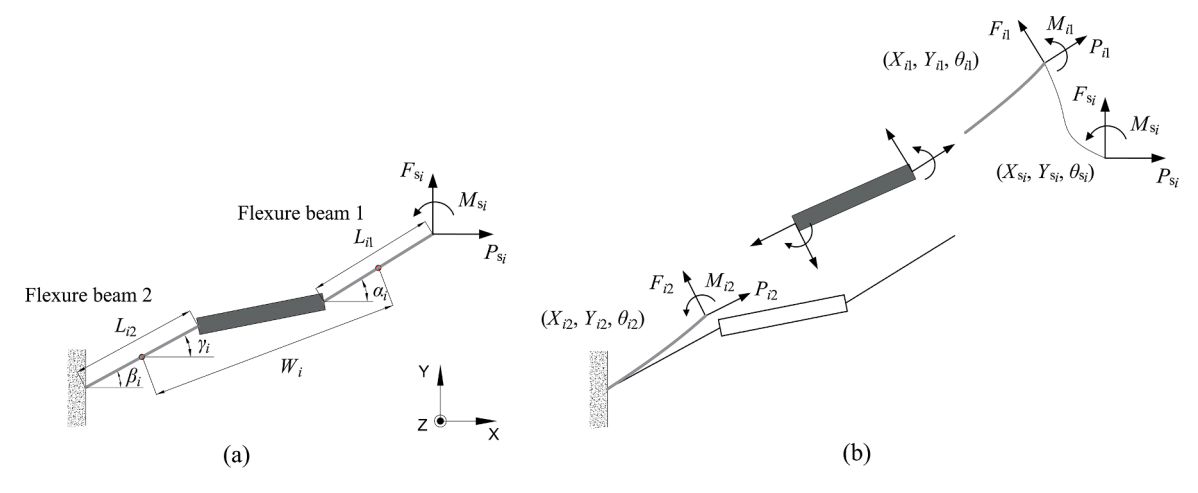


Fig. 1. Configuration of a general beam: (a) geometry parameters of the GLBM; (b) FBD of the general beam.

$$\begin{bmatrix}
F_{i1}L_{i1}^{2}/EI \\
M_{i1}L_{i1}^{2}/EI
\end{bmatrix} = \begin{bmatrix}
12 & -6 \\
-6 & 4
\end{bmatrix} \begin{bmatrix}
Y_{i1}/L_{i1} \\
\theta_{i1}
\end{bmatrix} + P_{i1}L_{i1}^{2}/EI \begin{bmatrix}
1.2 & -0.1 \\
-0.1 & 2/15
\end{bmatrix} \begin{bmatrix}
Y_{i1}/L_{i1} \\
\theta_{i1}
\end{bmatrix}$$

$$X_{i1}/L_{i1} = \left( \left( T_{i}/L_{i1}^{2} \right)^{2}/12 \right) \cdot \left( P_{i1}L_{i1}^{2}/EI \right) + 0.5[Y_{i1}/L_{i1} \theta_{i1}] \begin{bmatrix}
1.2 & -0.1 \\
-0.1 & 2/15
\end{bmatrix} \begin{bmatrix}
Y_{i1}/L_{i1} \\
\theta_{i1}
\end{bmatrix}$$

$$+ \left( P_{i1}L_{i1}^{2}/EI \right) [Y_{i1}/L_{i1} \theta_{i1}] \begin{bmatrix}
1/700 & -1/1400 \\
-1/1400 & 11/6300
\end{bmatrix} \begin{bmatrix}
Y_{i1}/L_{i1} \\
\theta_{i1}
\end{bmatrix}$$
(2)

The constitutive equations of flexure beam 2 can be expressed below.

In its deformed configuration, the tip displacement of the GLBM is generally the combination of the tip displacement of each beam in their local coordinates and the displacement caused by the rotation of the

$$\begin{bmatrix} F_{12}L_{12}^2/EI \\ M_{12}L_{12}^2/EI \end{bmatrix} = \begin{bmatrix} 12 & -6 \\ -6 & 4 \end{bmatrix} \begin{bmatrix} Y_{12}/L_{12} \\ \theta_{12} \end{bmatrix} + P_{12}L_{12}^2 / EI \begin{bmatrix} 1.2 & -0.1 \\ -0.1 & 2/15 \end{bmatrix} \begin{bmatrix} Y_{12}/L_{12} \\ \theta_{12} \end{bmatrix} 
X_{12}/L_{12} = \left( (T_i/L_{12}^2)^2/12 \right) \cdot \left( P_{12}L_{12}^2/EI \right) + 0.5[Y_{12}/L_{12} \ \theta_{12}] \begin{bmatrix} 1.2 & -0.1 \\ -0.1 & 2/15 \end{bmatrix} \begin{bmatrix} Y_{12}/L_{12} \\ \theta_{12} \end{bmatrix} 
+ (P_{12}L_{12}^2/EI)[Y_{12}/L_{12} \ \theta_{12}] \begin{bmatrix} 1/700 & -1/1400 \\ -1/1400 & 11/6300 \end{bmatrix} \begin{bmatrix} Y_{12}/L_{12} \\ \theta_{12} \end{bmatrix}$$
(3)

The force balance equations are derived based on the deformed configuration as shown in Fig. 1(b), which captures the contributions of the axial load to the bending moment.

$$\begin{bmatrix} P_{i1} \\ F_{i1} \end{bmatrix} = \begin{bmatrix} \cos(\alpha_{i} + \theta_{i2}) & \sin(\alpha_{i} + \theta_{i2}) \\ -\sin(\alpha_{i} + \theta_{i2}) & \cos(\alpha_{i} + \theta_{i2}) \end{bmatrix} \begin{bmatrix} P_{si} \\ F_{si} \end{bmatrix}$$

$$\begin{bmatrix} 0 \\ 0 \end{bmatrix} = \begin{bmatrix} \cos(\alpha_{i} + \theta_{i2}) & -\sin(\alpha_{i} + \theta_{i2}) \\ \sin(\alpha_{i} + \theta_{i2}) & \cos(\alpha_{i} + \theta_{i2}) \end{bmatrix} \begin{bmatrix} P_{i1} \\ F_{i1} \end{bmatrix} - \begin{bmatrix} \cos(\beta_{i}) & -\sin(\beta_{i}) \\ \sin(\beta_{i}) & \cos(\beta_{i}) \end{bmatrix} \begin{bmatrix} P_{i2} \\ F_{i2} \end{bmatrix}$$

$$M_{i1} - M_{si} = 0$$

$$M_{i1} + F_{i1}(X_{i1} + L_{i1}) - P_{i1}Y_{i1} - M_{i2} + (W_{i} \cdot \cos(\gamma_{i} + \theta_{i2}) - \cos(\beta_{i} + \theta_{i2}) \\ \cdot L_{i1}/2 - \cos(\alpha_{i} + \theta_{i2}) \cdot L_{i1}/2) \cdot (F_{i1} \cdot \cos(\alpha_{i} + \theta_{i2}) + P_{i1} \cdot \sin(\alpha_{i} + \theta_{i2}))$$

$$+ (W_{i} \cdot \sin(\gamma_{i} + \theta_{i2}) - \sin(\beta_{i} + \theta_{i2}) \cdot L_{i1}/2 - \sin(\alpha_{i} + \theta_{i2}) \cdot L_{i1}/2)$$

$$\cdot (F_{i1} \sin(\alpha_{i} + \theta_{i2}) - P_{i1} \cdot \cos(\alpha_{i} + \theta_{i2})) = 0$$

$$(4)$$

rigid stage in the global coordinate.

$$\begin{split} X_{i1} \cdot \cos(\alpha_{i} + \theta_{i2}) + X_{i2} \cdot \cos(\beta_{i}) - Y_{i1} \cdot \sin(\alpha_{i} + \theta_{i2}) - Y_{i2} \cdot \sin(\beta_{i}) \\ - 2 \cdot h_{0} \cdot \sin(\theta_{i2}/2) \cdot \cos(\pi/2 - \arcsin((W_{i} \cdot \sin(\gamma_{i}) - \sin\beta_{i} \cdot L_{i1}/2) \\ + \sin(\alpha_{i}) \cdot L_{i1}/2)/h_{0}) - \theta_{i2}/2) - X_{si} \\ &= 0 \ Y_{i1} \cdot \cos(\alpha_{i} + \theta_{i2}) + Y_{i2} \cdot \cos(\beta_{i}) + X_{i1} \cdot \sin(\alpha_{i} + \theta_{i2}) + X_{i2} \cdot \sin(\beta_{i}) \\ + 2 \cdot h_{0} \cdot \sin(\theta_{i2}/2) \cdot \sin(\pi/2 - \arcsin((W_{i} \cdot \sin(\gamma_{i}) - \sin\beta_{i} \cdot L_{i1}/2) \\ + \sin(\alpha_{i}) \cdot L_{i1}/2)/h_{0}) - \theta_{i2}/2) - Y_{si} \\ &= 0 \ \theta_{si} = \theta_{i} + \theta_{i2} \end{split}$$
(5)

where 
$$h_0 = \sqrt{(W_i \cdot \cos(\gamma_i) - \cos(\beta_i) \cdot L_{i1}/2 + \cos(\alpha_i) \cdot L_{i1}/2)^2 + (W_i \cdot \sin(\gamma_i) - \sin(\beta_i) \cdot L_{i1}/2 + \sin(\alpha_i) \cdot L_{i1}/2)^2}$$

The derivation of the force-displacement characteristic of the GLBM is based on the six constitutive equations (three each of the flexure beams), six force balance equations, and three geometry compatibility equations. When solving the system of equations, one can obtain the

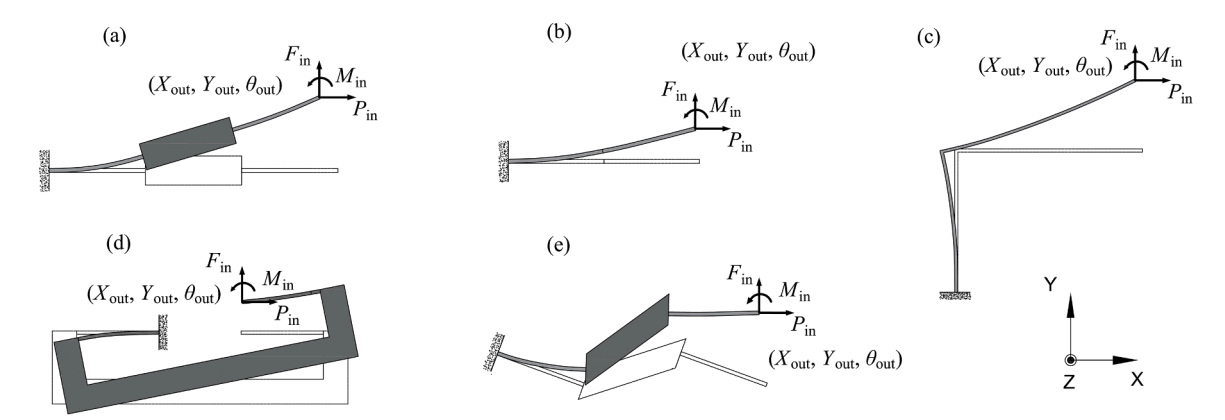


Fig. 2. GLBM in different configurations: (a) straight/conventional lumped-compliance beam; (b) distributed-compliance beam; (c) folded beam; (d) inverted beam; (e) inclined beam.

**Table 1**Geometric parameters of the five configurations for the GLBM.

Cases	$\alpha_i$ (deg)	$\beta_i$ (deg)	$\gamma_i$ (deg)	$W_i$ (mm)	$L_{i1}$ (mm)	$L_{i2}$ (mm)	$T_i$ (mm)	$U_i$ (mm)
1	0	0	0	10	10	4	0.4	20
2	0	0	0	10	10	4	0.4	10
3	0	90	33.70	20	30	4	0.4	18.03
4	180	-180	0	10	10	4	0.4	20
5	-20	-20	0	10	10	4	0.4	20

displacements  $(X_{sib} \ Y_{sib} \ \theta_{si})$  by giving the input force  $(F_{sib} \ P_{sib} \ M_{si})$ , and vice versa. Each GLBM contains 15 equations that govern the force-displacement characteristics. Using the GLBM to synthesize a complex structure that contains multiple general beams, the corresponding equations will be bulky. However, this issue can easily be solved in most existing mathematical software, i.e., Maple, MATLAB, and Mathematica by simply adding a loop function to repeat the force-displacement equations multiple times.

#### 3. FEA verification and parametric analysis

The GLBM offers a versatile approach to effectively model a general beam that incorporates any two flexure beams connected in series for various configurations. These general beam configurations are widely favored in the design of compliant mechanisms, owing to their widespread popularity and numerous advantages. We have compiled a list of some existing specific configurations as shown in Appendix B.

In this section, we focus on showcasing five representative configurations (Fig. 2) using the GLBM. To ensure the credibility of our findings, we conducted a thorough verification process by comparing the analytical results with those obtained from the nonlinear FEA tool.

These configurations, displayed in Fig. 2, are widely adopted in the design of compliant mechanisms. For instance, the inverted beam and the inclined beam, shown in Fig. 2(d) and (e), respectively, are frequently employed in the design of bistable mechanisms [63,64,14,65-67] and translational joints [68,19], whereas the folded beam, presented in Fig. 2(c) is commonly used in the design of flexure joints [69,70]. Additionally, the distributed-compliance beam and the straight lumped-compliance beam, which are among the most popular building blocks, are also utilized in various applications. The geometry parameters of each configuration are shown in Table 1. Each configuration (beam) was subjected to generalized end-loads ( $F_{\rm in}$ ,  $P_{\rm in}$ ,  $M_{\rm in}$ ), resulting in end displacements ( $X_{\rm out}$ ,  $Y_{\rm out}$ , and  $\theta_{\rm out}$ ) with respect to the global coordinates X-Y-Z.

The FEA simulations were performed in commercial software COMSOL@5.0. A general flowchart depicting the FEA simulation process with Comsol software is presented in Fig. 3. In line with the

assumptions made in the analytical model, the stages and frames were set as rigid, and no fillet was added around the sharp corner. However, it is important to avoid sharp corners in the connection area between the rigid part and the flexure, as these can cause stress singularities. In this instance, a finer mesh did not result in superior outcomes. Therefore, it may be necessary to perform a singularity check to ensure that the results converge.

## 3.1. FEA verification of GLBM in different configurations

By incorporating the relevant parameters into the GLBM derived in Section 2, we can obtain an analytical model that governs the force-displacement characteristics of each case, subject to generalized end-loads. To comprehensively study the force-displacement characteristic, a relatively large force is applied to the beams to induce a substantial displacement.

Fig. 4 presents a comparison between the analytical model and FEA simulation results in terms of the force-displacement relationship for the straight lumped-compliance beam. The analytical model was able to predict the resulting displacements in each direction ( $X_{\rm out}$ ,  $Y_{\rm out}$ , and  $\theta_{\rm out}$ ) with a prominent level of accuracy, as evidenced by the close agreement between the analytical and FEA results. The maximum error between the analytical and FEA results was 4.93 % for the transverse displacement ( $Y_{\rm out}$ ) in Fig. 4(b), which reached 54 % of the beam length (30 mm). For the axial displacement ( $X_{\rm out}$ ) and tip rotation ( $\theta_{\rm out}$ ) in Fig. 4(a) and (c), respectively, the maximum errors were 4.48 % and 5.85 %, respectively. Generally, a smaller displacement resulted in a better correlation between the analytical and FEA results. These findings validate the reliability of the analytical model in predicting the force-displacement behavior of the straight lumped-compliance beam.

The results of the distributed-compliance beam are plotted in Fig. 5 where the error is below 4.71 % for the tip rotation. When the axial displacement reaches 2.4 mm (beam length 20 mm), it produces a maximum error of 2.27 % between the FEA and analytical results as shown in Fig. 5(c). A force combination of  $F_{\rm in} = 2$  N,  $P_{\rm in} = -0.8$  N,  $M_{\rm in} = 0.04$  Nm produces a transverse displacement ( $Y_{\rm out}$ ) of 8.43 mm with a maximum error of 3.77 %, which is illustrated in Fig. 5(b).

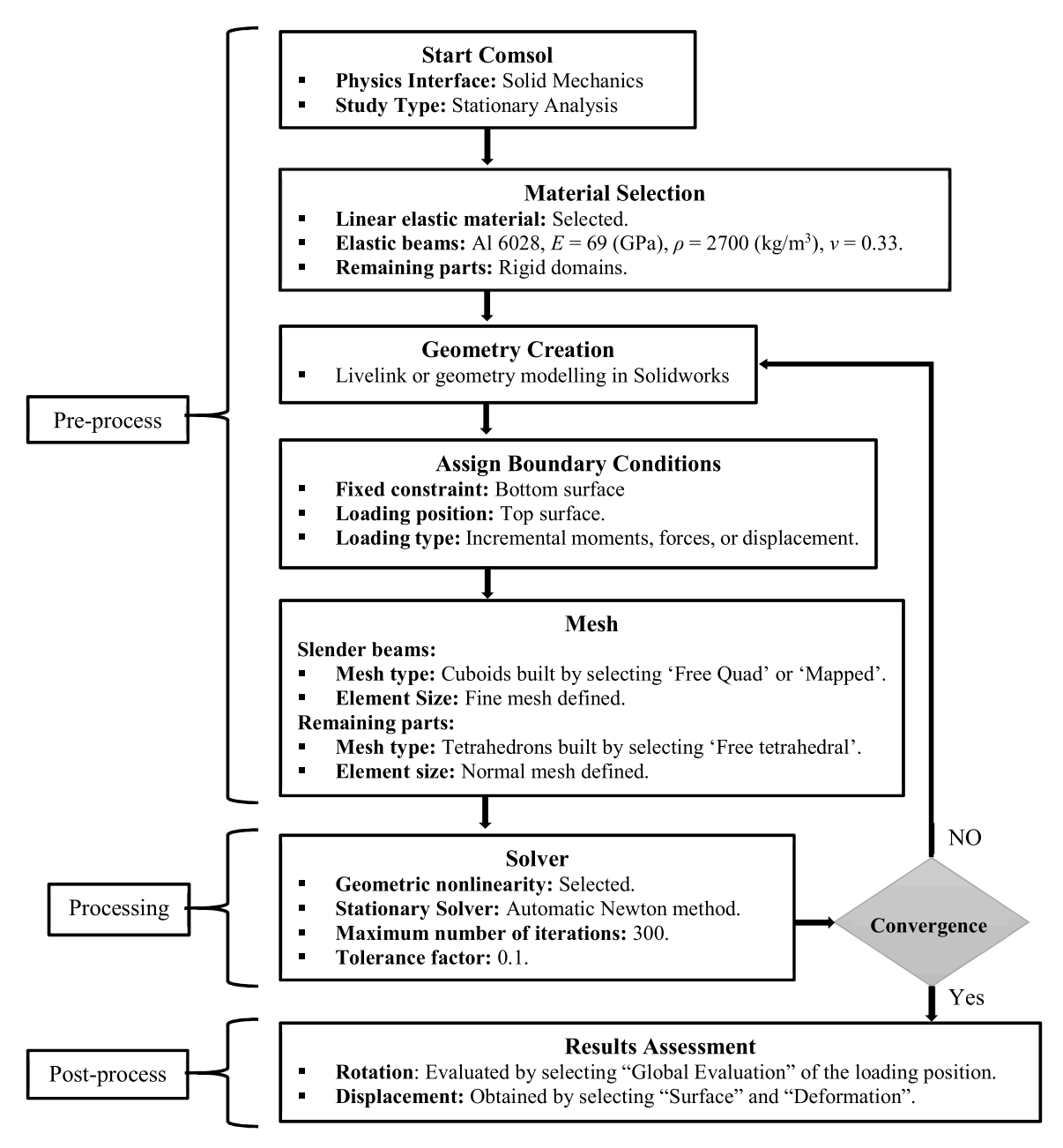
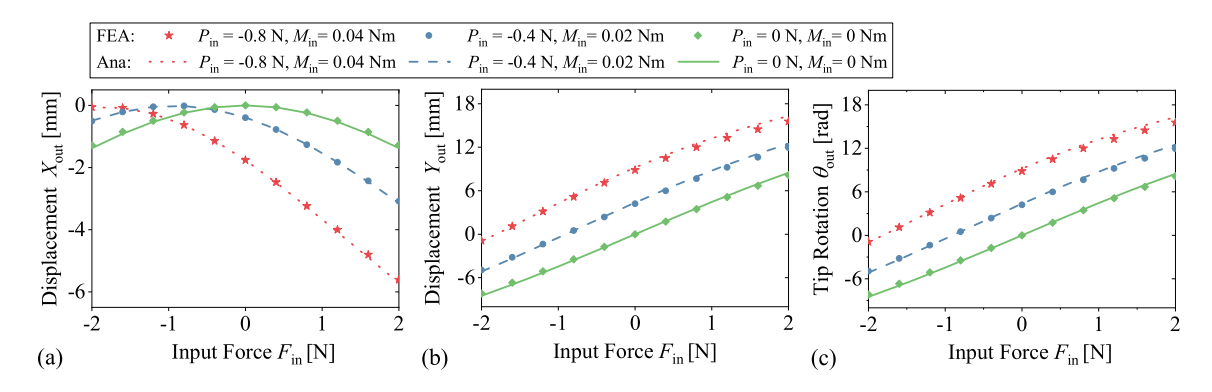
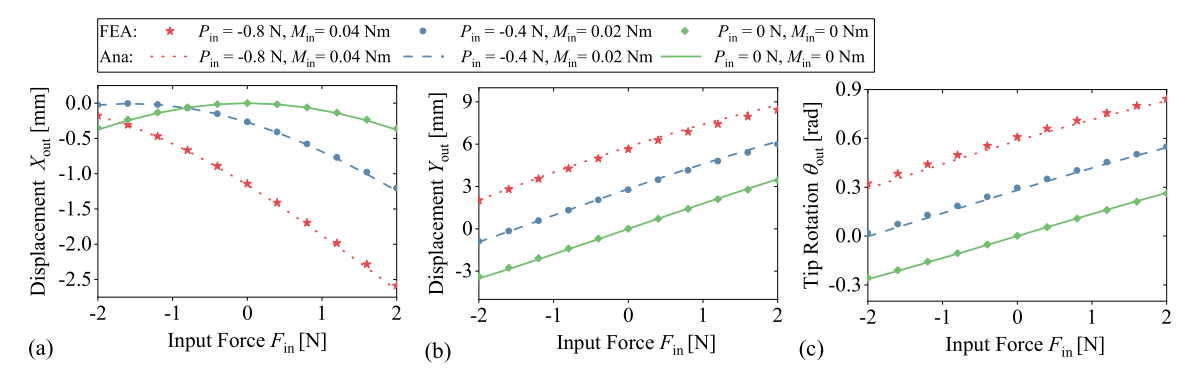


Fig. 3. Flowchart of the process of FEA simulation based on the software Comsol.



**Fig. 4.** FEA verification of the lumped-compliance beam: (a) displacement in *X*-direction versus the input force  $F_{\rm in}$ ; (b) displacement in *Y*-direction versus the input force  $F_{\rm in}$ ; (c) rotation about *Z*-axis versus the input force  $F_{\rm in}$ .



**Fig. 5.** FEA verification of the distributed-compliance beam: (a) displacement in *X*-direction versus the input force  $F_{in}$ ; (b) displacement in *Y*-direction versus the input force  $F_{in}$ ; (c) rotation about *Z*-axis versus the input force  $F_{in}$ .

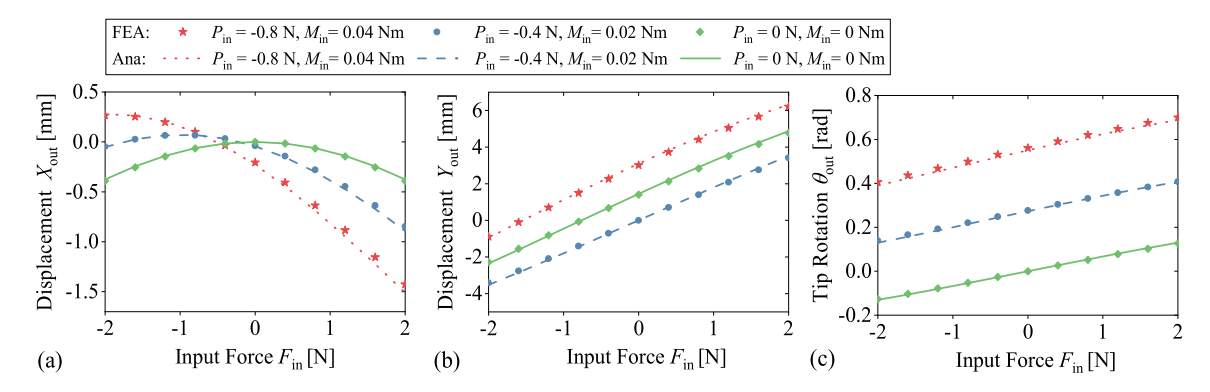


**Fig. 6.** FEA verification of the inverted beam: (a) displacement in *X*-direction versus the input force  $F_{\rm in}$ ; (b) displacement in *Y*-direction versus the input force  $F_{\rm in}$ ; (c) rotation about *Z*-axis versus the input force  $F_{\rm in}$ .

The comparison between the analytical and FEA results of case 3 (inverted beam) is plotted in Fig. 6. The maximum error that occurs in the tip rotation is 3.12 % while the maximum error for the transverse displacement (Fig. 6(b)) and axial displacement (Fig. 6(a)) is 4.69 % and 2.64 %, respectively. Fig. 7 presents the comparison of the results for case 4 (inclined beam). While the beam yields 16.82 mm in the transverse direction ( $Y_{\rm out}$ ), it has a maximum error of 4.98 %. The maximum error between the analytical results and FEA results, in this case, is 4.28 % (for  $\theta_{\rm out}$ ) and 5.75 % (for  $X_{\rm out}$ ).

Fig. 8(a) displays the force-displacement characteristic of the folded beam, with a maximum error of 4.48 % observed between the analytical and FEA results in terms of axial displacement. The transverse displacement and tip rotation exhibit errors of 2.75 % and 5.41 %, which are depicted in Fig. 8(b) and (c), respectively.

In Section 3.1, we utilized the developed GLBM to model five

representative flexure beam units. We verified the results by comparing them with those obtained from an FEA tool. Our analysis revealed that the error between the analytical results and the FEA results was in the range of 2 % to 6 % for a large deflection (transverse displacement over 40 % of the beam length). Overall, the results suggest that the GLBM is effective in predicting the force-displacement behavior in any configuration, with reasonable accuracy as compared to the FEA simulations.

## 3.2. Parametric analysis

A parametric analysis is performed to analyze the influence of geometric parameters on the stiffness of a general lumped-compliance beam. This analysis helps in evaluating trade-offs between different design options and making informed decisions during certain compliant mechanism design processes. The analysis was implemented and

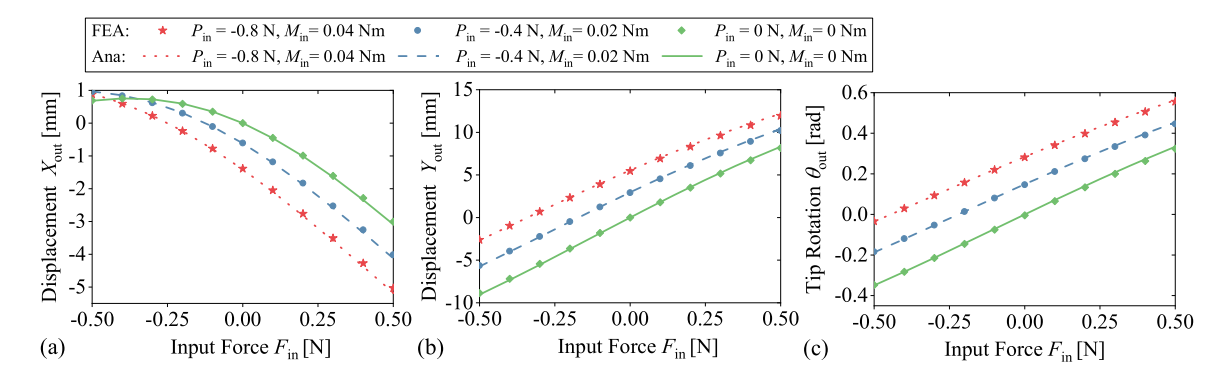


**Fig. 7.** FEA verification of the inclined beam: (a) displacement in *X*-direction versus the input force  $F_{in}$ ; (b) displacement in *Y*-direction versus the input force  $F_{in}$ ; (c) rotation about *Z*-axis versus the input force  $F_{in}$ .

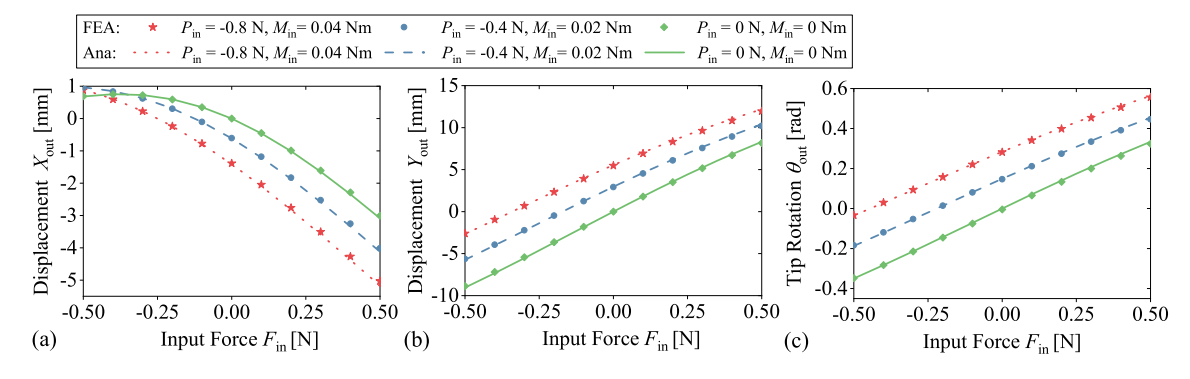


**Fig. 8.** FEA verification of the folded beam: (a) displacement in *X*-direction versus the input force  $F_{\rm in}$ ; (b) displacement in *Y*-direction versus the input force  $F_{\rm in}$ ; (c) rotation about *Z*-axis versus the input force  $F_{\rm in}$ .

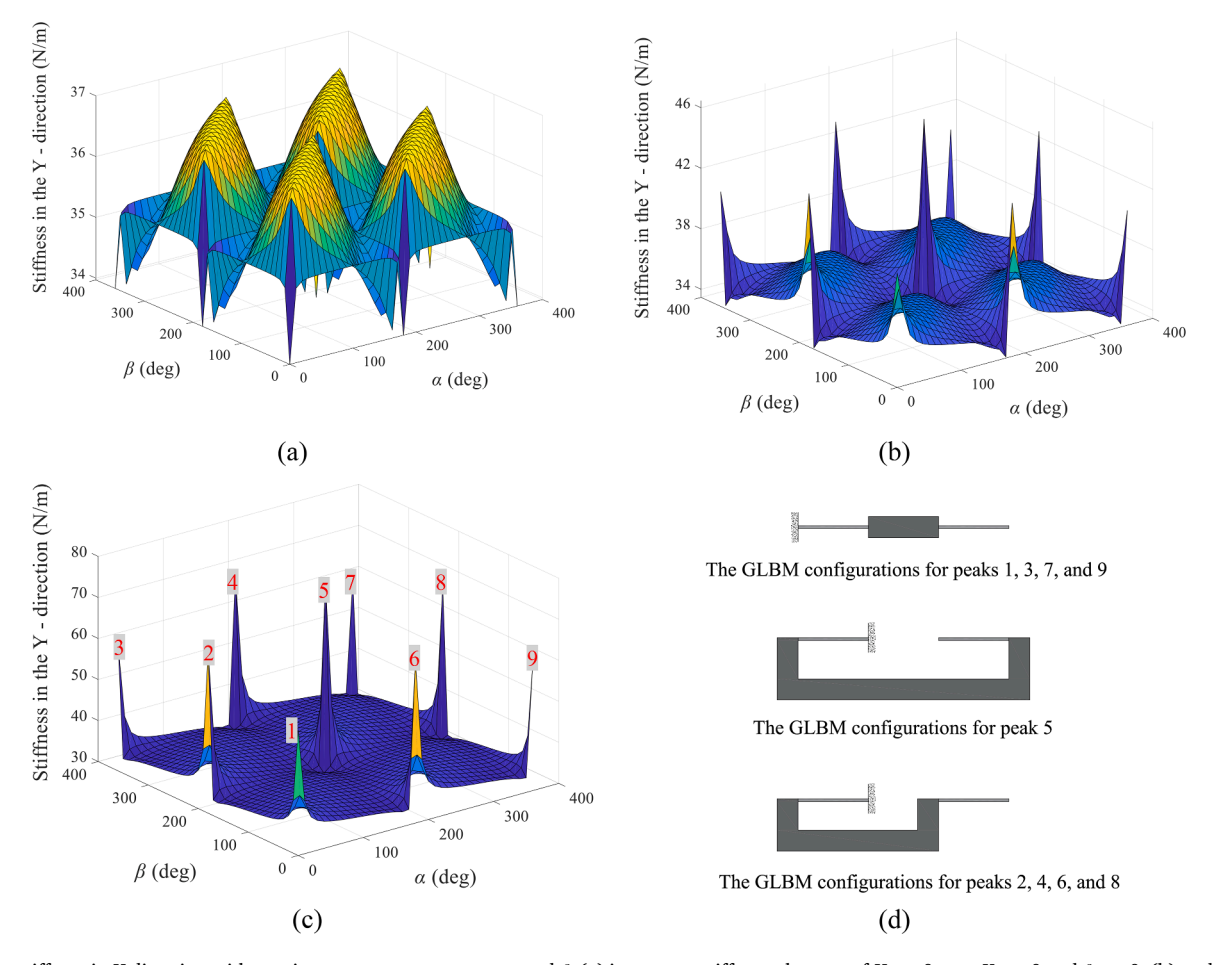


Fig. 9. The stiffness in Y-direction with varying geometry parameters  $\alpha$  and  $\beta$ : (a) instantons stiffness, the case of  $Y_{\rm in}=0$  mm,  $X_{\rm in}=0$  and  $\theta_{\rm in}=0$ ; (b) under the case of  $Y_{\rm in}=0.1$  mm,  $X_{\rm in}=0$  and  $\theta_{\rm in}=0$ ; (c) under the case of  $Y_{\rm in}=0.2$  mm,  $X_{\rm in}=0$  and  $\theta_{\rm in}=0$ ; (d) and the general beam configurations for each peak.

## computed using Matlab.

Specifically, the geometric parameters  $\alpha_1$  and  $\beta_1$  were chosen as variables, ranging from  $0^\circ$  to  $360^\circ$  with increments of  $10^\circ$ , to investigate the changes in stiffness along the *Y*-direction. And the rest parameters are defined as  $L_{11} = L_{12} = 10$  mm,  $\gamma_1 = 0$  deg and  $W_1 = 20$  mm. By applying input displacements and solving the system of equations, the stiffness was determined. Fig. 9(a) depicts the stiffness with a neglective input displacement of  $10^{-5}$  mm in the *Y*-direction. Fig. 9(b) illustrates the stiffness for a given input displacement of  $Y_{\rm in} = 0.1$  mm,  $X_{\rm in} = 0$  and  $\theta_{\rm in} = 0$ . Fig. 9(c) illustrates the stiffness for a given input displacement of  $Y_{\rm in} = 0.2$  mm,  $X_{\rm in} = 0$  and  $\theta_{\rm in} = 0$ . The input only occurs in the *Y*-direction, which mimics the single-leg motion of the symmetrical

traditional translational joint [68].

Fig. 9(a) clearly illustrates the variation in stiffness at a small scale, ranging from 34 N/mm to 37 N/mm, when subjected to a negligible input of  $10^{-3}$  mm in the *Y*-direction. However, as we increase the input displacement to 0.1 mm and 0.2 mm, the stiffness of different GLBM configurations exhibits a significant variation, ranging from 34 N/mm to 44 N/mm and from 34 N/mm to 65 N/mm, respectively.

Fig. 9(d) presents the corresponding GLBM configurations of each peak in Fig. 9(b) and (c). Notably, the GLBM designs featuring colinear flexure beams, such as the inverted beam and the lump-compliance beam, exhibit higher stiffness compared to the GLBM designs with non-colinear flexure beams, such as the folded beam and inclined beam.

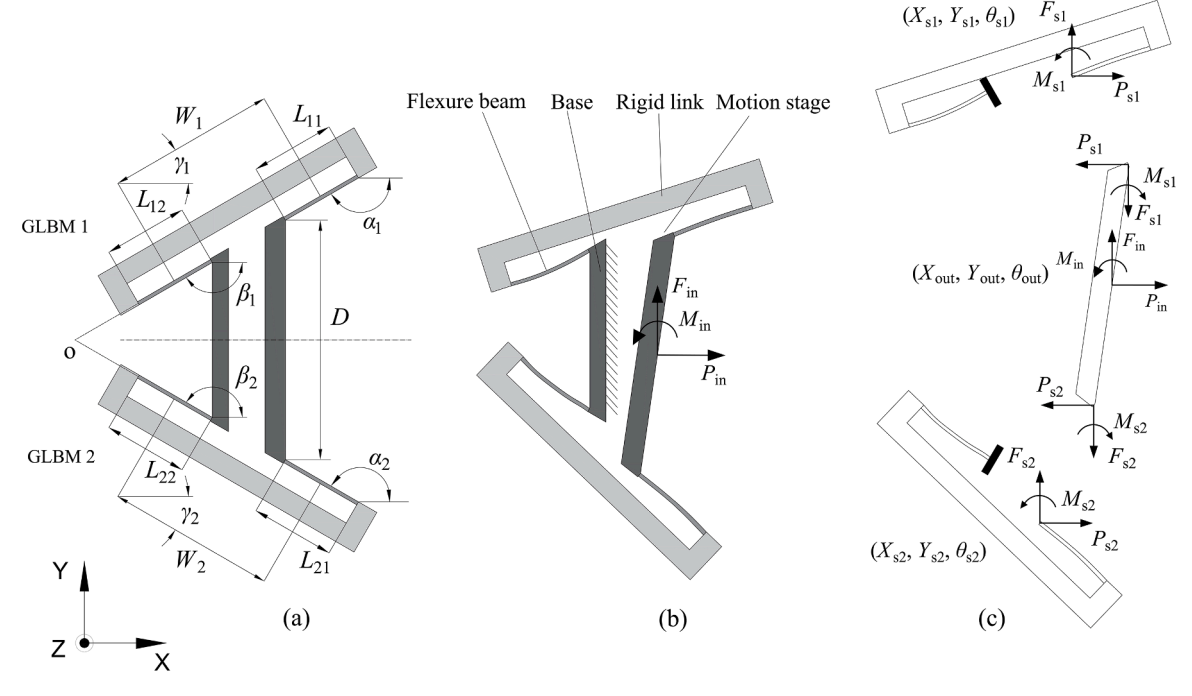


Fig. 10. Revolute joint with inverted beams: (a) geometry; (b) deformed configuration; (c) FBD of the joint.

**Table 2**The geometric parameters of the revolute joint.

	•							
GLBM 1	$\alpha_1$ (deg)	$\beta_1$ (deg)	$\gamma_1$ (deg)	W <sub>1</sub> (mm)	L <sub>11</sub> (mm)	L <sub>12</sub> (mm)	<i>T</i> <sub>1</sub> (mm)	<i>U</i> <sub>1</sub> (mm)
GLDIVI I	-150	210	30	40	20	20	0.4	4
GLBM 2	$a_2$ (deg)	$\beta_2$ (deg)	$\gamma_2$ (deg)	$W_2$ (mm)	$L_{21}$ (mm)	$L_{22}$ (mm)	$T_2$ (mm)	$U_2$ (mm)
GLDIVI Z	150	-210	-30	40	20	20	0.4	4

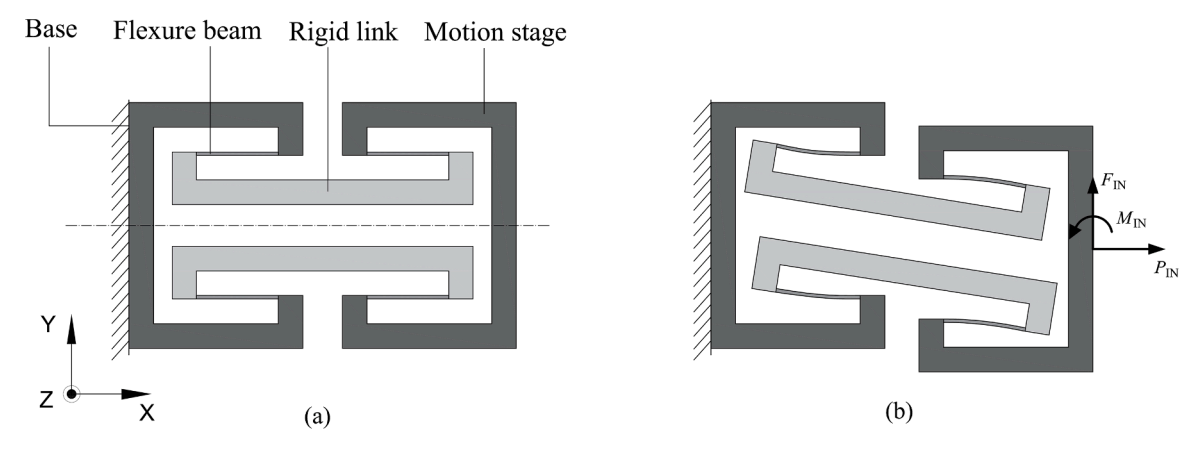


Fig. 11. Translational joint derived from the revolute joint [65]: (a) geometric composition; (b) deformed configuration.

Furthermore, an interesting observation from Fig. 9 is that the load-dependent effect is not prominent in the GLBM designs with parallel but not colinear flexure beams. This can be attributed to the minimal compression or tensile forces experienced by the flexure beams when subjected to small input displacements. In these configurations, the displacement in the X-direction and tip rotation remains zero while a displacement is applied in the Y-direction. However, it is worth noting that the GLBM model with colinear beams experiences significant tensile forces even for small displacements. The load-dependent effect is also observed by comparing Fig. 9(a) and (b). Fig. 9(b) shows a larger value while the input displacement  $Y_{\rm in}$  increases.

The parametric analysis conducted in this study incorporates the

variables  $\alpha$  and  $\beta$  to examine the impact of various GLBM configurations on stiffness. Remarkably, this approach enables simultaneous analysis of thousands of configurations, with each analysis requiring only 30 s of computing time in Matlab. This level of efficiency surpasses that of FEA simulation software and proves to be highly advantageous for the parametric optimization of compliant mechanisms.

## 4. Application to design compliant mechanisms

In this Section, the proposed GLBM was used to synthesize two different cases, namely, the revolute joint and the bistable mechanism. To analyze the force-displacement characteristics of each compliant

mechanism, we need to format a system of equations consisting of the GLBM, force equilibrium, and geometry compatibility. The system equations are solved in Maple using *Fsolve* function and the obtained results are further verified by the FEA tool using Comsol. The process of the FEA simulation generally follows the same process presented in Fig. 3.

#### 4.1. Case I - revolute Joint with two identical inverted beams

Fig. 10 illustrates the revolute joint design using an inverted beam with specific geometry parameters, which are listed in Table 2. By simply changing the value of these parameters, we can quickly model a translational joint as shown in Fig. 11 [71]. This allows for quick and efficient design iterations, reducing development time. In this case study, the revolute joint is being utilized as the subject of analysis.

The revolute joint with inverted beams is typically capable of withstanding a large compression force. In this case, the flexure beam only suffers tensile force which avoids buckling [71]. To derive the force balance equation, we will begin by analyzing the FBD, along with the GLBM and geometry compatibility. By combining these mechanics, we can obtain a system of equations that govern the force-displacement characteristics of the revolute joint.

Fig. 10(a) and (b) illustrate the geometry and the deformed configuration under given end forces, respectively. We then substituted the corresponding geometry parameters as shown in Table. 2, into the GLBM to extract the constitutive equations of the inverted beams. It is important to note that each of the inverted beams has its own GLBM, as derived previously. With the constitutive equation in hand, we then continued with the force equilibrium analysis and geometry compatibility to gain a deeper understanding of the revolute joint.

Based on the FBD (Fig. 10(c)), we can obtain the force equilibrium:

$$\begin{split} F_{\text{in}} &= F_{\text{s1}} + F_{\text{s2}} \\ P_{\text{in}} &= P_{\text{s1}} + P_{\text{s2}} \\ M_{\text{in}} &= M_{\text{s1}} + M_{\text{s2}} - P_{\text{s2}} \cdot \cos(\theta_{\text{out}}) \cdot D/2 - F_{\text{s2}} \cdot \sin(\theta_{\text{out}}) \cdot D/2 + P_{\text{s1}} \cdot \cos(\theta_{\text{out}}) \cdot D/2 \\ + F_{\text{s1}} \cdot \sin(\theta_{\text{out}}) \cdot D/2 \end{split}$$

$$(6)$$

where D = 50 mm is the length of the motion stage.

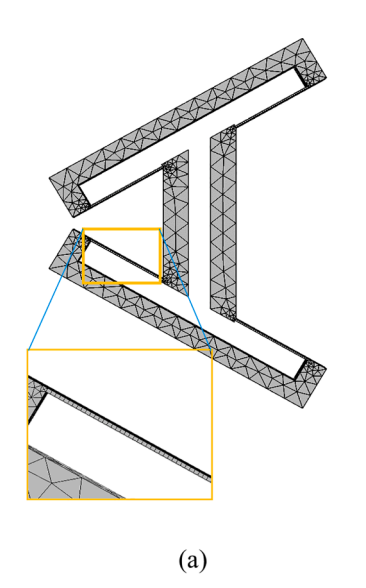
The geometry compatibility conditions for the revolute joint are shown below:

$$\begin{split} X_{s1} &= X_{\text{out}} + \sin(\theta_{\text{out}}) \cdot D/2; \ X_{s2} = X_{\text{out}} - \sin(\theta_{\text{out}}) \cdot D/2; \ Y_{s1} = Y_{\text{out}} + (1 \\ &- \cos(\theta_{\text{out}}) \cdot D/2); Y_{s2} \\ &= Y_{\text{out}} - (1 - \cos(\theta_{\text{out}}) \cdot D/2); \theta_{s1} = \theta_{\text{out}}; \ \theta_{s2} = \theta_{\text{out}} \end{split}$$
 (7)

To gain insight into the force-displacement characteristics of the revolute joint, a system of nonlinear equations was developed. Among them, 30 equations were governed by two GLBMs responsible for describing the force-displacement characteristics, and constitutive conditions of the resulting compliant mechanism. The remaining 9 equations comprised three force-equilibrium equations and 6 geometry compatibility equations. This analytical model was then used to validate our findings with the FEA tool, Comsol. By comparing the results obtained from both the analytical model and the FEA tool, we were able to obtain a more comprehensive understanding of the force-displacement behavior of the revolute joint. This approach allowed us to verify the accuracy of our model and identify any discrepancies or limitations that may exist in the analytical or computational methods used. Incremental input forces including  $F_{\rm in}$ ,  $P_{\rm in}$ , and  $M_{\rm in}$  are applied to the input stages with 10 steps. Calculation of the 10 steps together takes about 3-5 s using the Loop function in Maple, while the calculation using the FEA method takes about 80-85 s.

Fig. 12 depicts the mesh type and deformed configuration of the revolute joint in the FEA simulation. In Fig. 12(a), the rigid parts utilize default tetrahedral elements, while the flexure parts employ cuboid elements. This combination optimizes the element count, achieving a balance between computing time and accuracy without compromising the results. The displacement plot in Fig. 12(b) illustrates the outcome of applying an input force of 0.8 N in the Y-direction. As a result, the motion stage undergoes a significant displacement of 2.11 mm along the Y-direction.

Fig. 13 illustrates a comparison between the analytical results and the FEA simulation of the output displacement of the motion stage. The comparison shows good agreement between the two methods. Specifically, Fig. 13(a) presents the results of the motion stage rotation ( $\theta_{\rm out}$ ), with a maximum error between the analytical results and FEA simulation of 4.1 %. Fig. 13(b) plots the out displacement in the *X*-direction of the revolute joint under incremental input forces, demonstrating a nonlinear characteristic with a maximum error of 4.3 %. Finally, Fig. 13 (c) depicts the output displacement in the *Y*-direction, with an error between the analytical results and FEA results of less than 2.0 %. Overall, these results indicate the accuracy and reliability of both analytical and FEA methods in analyzing the behavior of the revolute



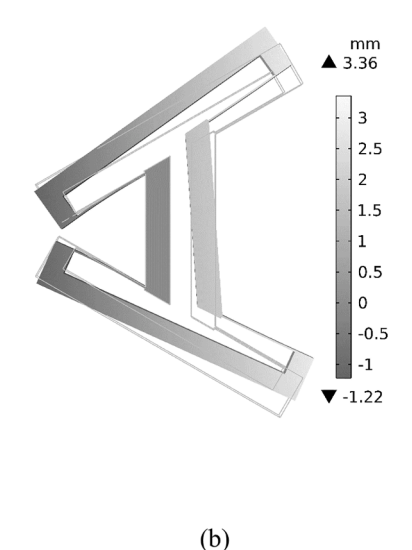
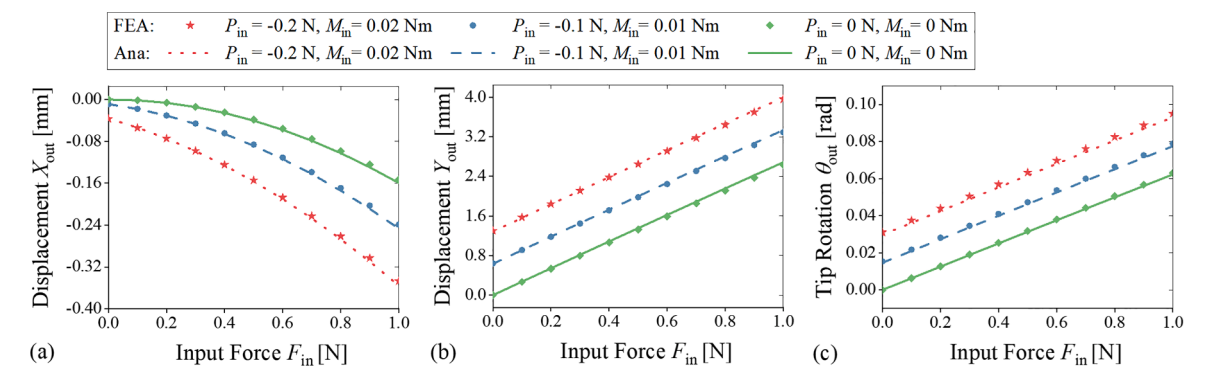
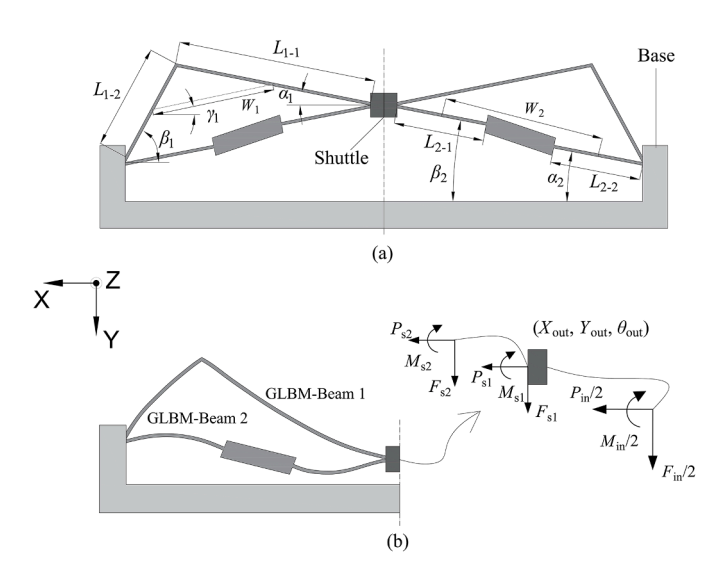


Fig. 12. FEA simulation in Comsol: (a) mesh type for the rigid bodies and flexure beams; (b) displacement plot of the revolute joint in Comsol.



**Fig. 13.** FEA verification of the revolute joint with inverted beam: (a) displacement in *X*-direction versus the input force  $F_{\rm in}$ ; (b) displacement in *Y*-direction versus the input force  $F_{\rm in}$ ; (c) rotation about *Z*-axis versus the input force  $F_{\rm in}$ .

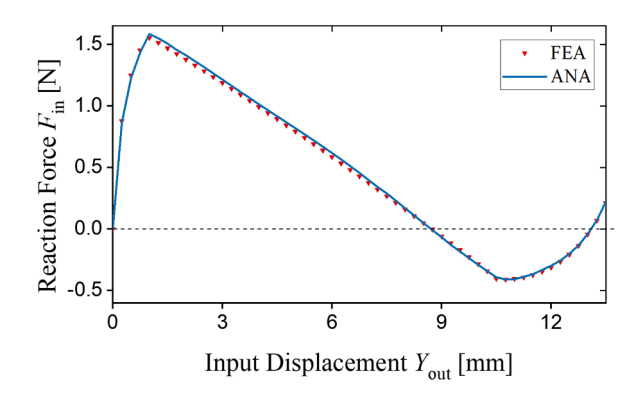


**Fig. 14.** Bistable mechanism with increased out-of-plane stiffness: (a) geometry parameters; (b) deformed configuration and the FBD of the shuttle.

joint.

## 4.2. Case II - bistable mechanism using two types of GLBMs

A novel bistable mechanism with triangle shape flexure [72] in which torsion reinforce structures are used to increase the out-of-plane stiffness as depicted in Fig. 14. It is mainly composed of a folded beam



 $\textbf{Fig. 16.} \ \ \textbf{FEA} \ \ \textbf{verification of the behavior of the bistable mechanism.}$ 

 Table 3

 The geometry parameters of the bistable mechanism.

GLBM 1	$a_1$ (deg) $-25.68$	$\beta_1$ (deg) 42.18	γ <sub>1</sub> (deg) 12.53	W <sub>1</sub> (mm) 18.69	L <sub>11</sub> (mm) 20	L <sub>12</sub> (mm) 25	T <sub>1</sub> (mm) 0.4	<i>U</i> <sub>1</sub> (mm) 4
GLBM 2	$\alpha_2$ (deg) 11	$\beta_2$ (deg) 11	γ <sub>2</sub> (deg) 13.65	W <sub>2</sub> (mm) 22.42	L <sub>21</sub> (mm) 15	L <sub>22</sub> (mm) 15	T <sub>2</sub> (mm) 0.4	<i>U</i> <sub>2</sub> (mm) 4

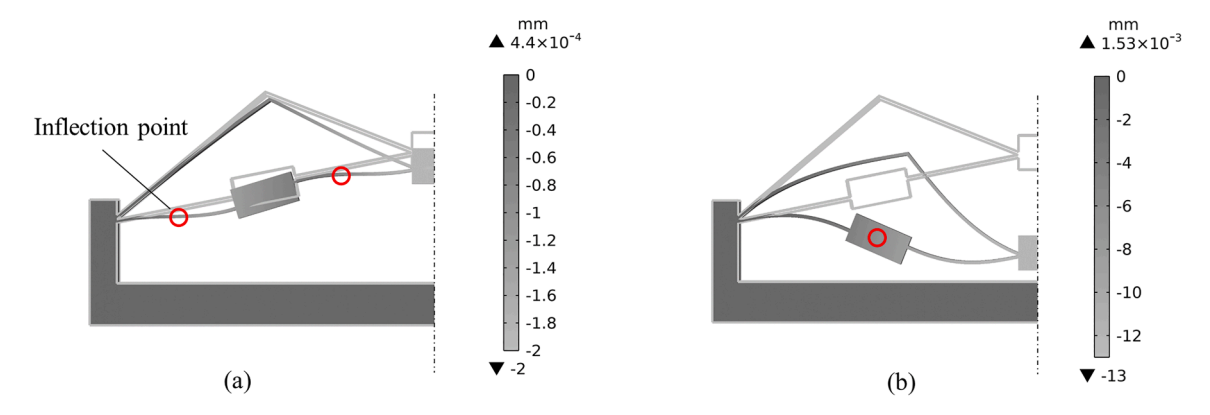


Fig. 15. Inflection points simulated in Comsol with one inflection point vanishing during snap-through: (a) bending with two inflection points; (b) the second bistable position with only one inflection point.

(GLBM 1) and an inclined beam (GLBM 2), shuttle and base. The folded beam is used to increase the torsional stiffness of the shuttle along the X-axis. To prevent self-retraction, the inclined beam is used to increase the strain energy stored in the second stable position and also to prevent the model from getting a higher buckling mode compared to the distributed-compliance beam. Fig. 14(b) displays the labeled geometry parameters of the bistable mechanism, while Table 3 presents their corresponding values.

To model this bistable mechanism, it is necessary to establish the constitutive, force equilibrium, and geometry compatibility conditions. This process is identical to the one presented in case one. Section 2 provides the derivation of the constitutive equation for each GLBM. Meanwhile, the force equilibrium can be obtained by the given FBD in Fig. 14(b), which is shown below.

$$F_{\rm in}/2 = -(F_{\rm s1} + F_{\rm s2}); \ P_{\rm in}/2 = -(P_{\rm s1} + P_{\rm s2}); \ M_{\rm in}/2$$
$$= M_{\rm s1} + M_{\rm s2} - (F_{\rm s1} + F_{\rm s2}) \cdot D/2 \tag{8}$$

where D=10 mm is the length of the shuttle, as labelled in Fig. 14(b). The geometry compatibility conditions for the bistable mechanism are shown below:

$$X_{s1} = 0; X_{s2} = 0; Y_{s1} = -Y_{out}; Y_{s2} = -Y_{out}; \theta_{s1} = 0; \theta_{s2} = 0$$
 (9)

The force-displacement characteristic of the bistable mechanism now can be obtained by solving the system of nonlinear equations derived above. The shuttle is subjected to incremental displacement to activate its bistable mechanism, which is also simulated in the FEA analysis.

The bistable mechanism's FEA simulation was conducted using Comsol, following a process similar to that presented in Fig. 3. It's noted that achieving convergence for the solution requires setting an appropriate iteration number, especially when dealing with significant nonlinear deformations. For this study, the maximum iteration number was set to 200 (default is 25). During the simulation, a critical buckling force was determined, causing the beam to buckle into a bending mode [70]. The shape taken by the buckled mechanism is defined by the number of inflection points. Fig. 15(a) visually illustrates the deformed shape of the bistable mechanism, which exhibits two inflection points before the snap-through position. However, after passing this

snap-through position, the mechanism moves towards its second stable position. Fig. 15(b) shows the deformed shape with only one inflection point.

Fig. 16 depicts a comparison of the analytical and FEA results, revealing good agreement between the two. The maximum absolute error in the reaction force is found to be below 0.035 N, validating the accuracy of the developed model in precisely modeling bistable mechanisms with both large deflections and high axial forces.

#### 5. Experimental validation of the revolute joint

In this section, we conducted an experimental test to validate both the FEA and analytical results of the revolute joint, as shown in Fig. 17. To ensure a robust experiment setup, we fabricated a prototype with specific parameters outlined in Table 4. The flexure beams were made from copper, and all other components were 3D printed by Ultimaker S3 using Polylactic Acid (PLA) as material. We employed an auxiliary positioning frame depicted in Fig. 17(b) to achieve precise assembly of the revolute joint to the 3D printed parts. The flexure beams were securely fixed to the rigid parts using super glue.

#### 5.1. Experimental setup of the revolute joint

Fig. 17(a) illustrates the experimental setup used to evaluate the force-displacement characteristics of the revolute joint under different loading conditions. The setup comprises five key components: a micrometer, a force sensor, a linear guide, the fabricated prototype, and a pulley system. The micrometer enabled us to precisely control and apply prescribed input displacements, while the force sensor, sitting on a linear guide, measured the reaction force from the motion stage. We utilized a pulley system to apply 100-gram and 200-gram weights acting payloads ( $P_{\rm in}$ ) to the motion stage in addition to the exerted input force from the micrometer. Fig. 17(c) showcases the deformed configuration of the revolute joint with a 200-gram payload. To ensure the reliability of our results, each experimental procedure was repeated three times, and the average of the experiment results was calculated for plot and comparison.

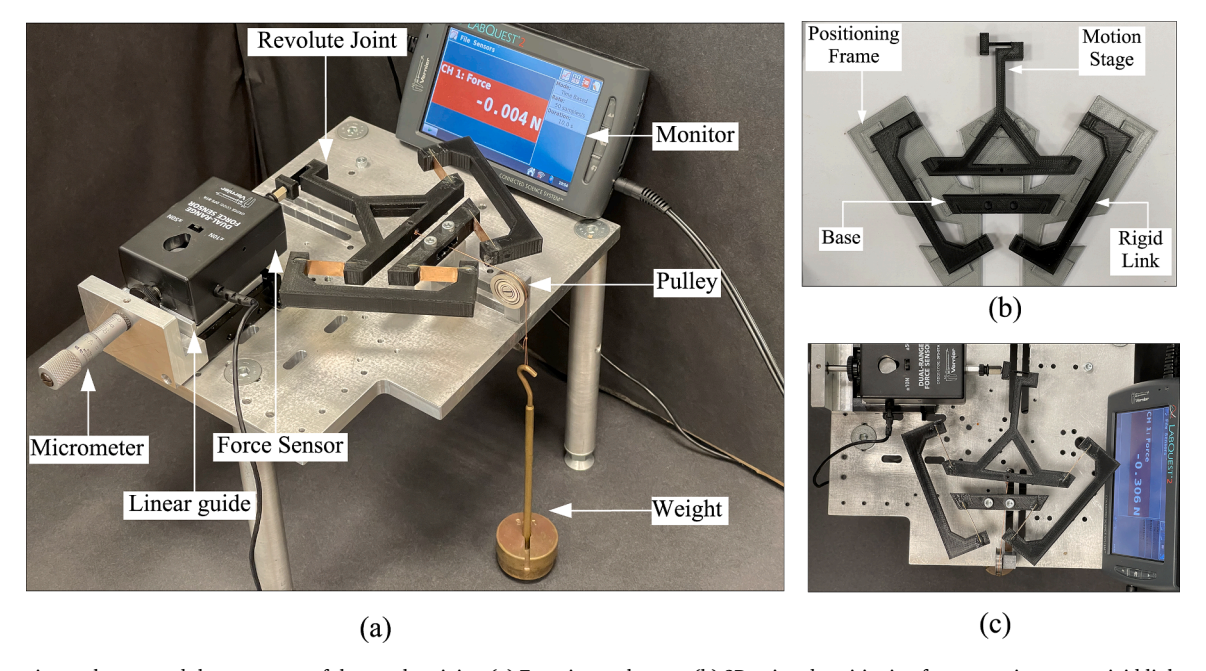


Fig. 17. Experimental setup and the prototype of the revolute joint: (a) Experimental setup; (b) 3D-printed positioning frame, motion stage, rigid link, and base; (c) its deformed configuration.

**Table 4**The geometric parameters of the fabricated revolute joint prototype.

GLBM 1	$\alpha_1$ (deg) $-150$	$\beta_1$ (deg) 210	$\gamma_1$ (deg) 30	W <sub>1</sub> (mm) 52	L <sub>11</sub> (mm) 20	L <sub>12</sub> (mm) 20	<i>T</i> <sub>1</sub> (mm) 0.3	<i>U</i> <sub>1</sub> (mm) 10
GLBM 2	$\alpha_2$ (deg) 150	$eta_2$ (deg) $-210$	$\gamma_2$ (deg) $-30$	W <sub>2</sub> (mm) 52	L <sub>21</sub> (mm) 20	L <sub>22</sub> (mm) 20	T <sub>2</sub> (mm) 0.3	U <sub>2</sub> (mm) 10

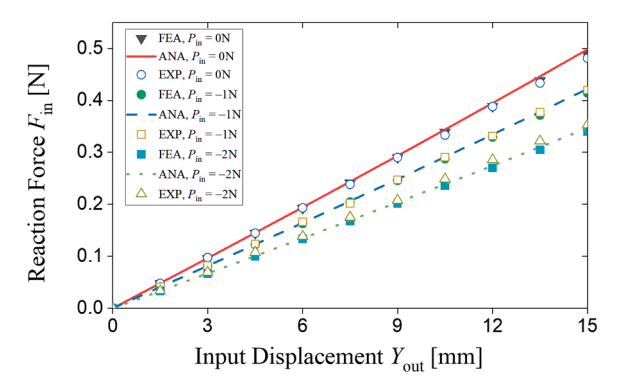


Fig. 18. Tip force-displacement characteristics under different payload.

#### 5.2. Experimental results

The experiment was carried out successfully to validate both the FEA and analytical results. Fig. 18 shows the tip force-displacement characteristics of the revolute joint under different payloads. As expected, the experimental results align closely with both the FEA and analytical results, demonstrating a maximum error of  $5.6\,\%$ . Notably, the revolute joint displays a load-dependent effect, where an increase in payload leads to a reduction in the rotational stiffness of the joint.

#### 6. Experimental validation of the bistable mechanism

In this section, we conducted experiments on a new bistable mechanism as shown in Fig. 19. To create a cost-effective experimental setup, we fabricated a monolithic 3D-printed prototype (Fig. 19(b)) and assembled it on the testing apparatus. The prototype was printed using the Ultimaker S3, with a layer height of 0.1 mm. PLA was used as the material, with a Young's modulus of 3.3 GPa and a Yield strength of 52.5 MPa. The experiment was carried out within the yield strength which is first simulated in the Comsol. The new bistable mechanism comprises two identical bistable mechanisms, each of which was previously presented in Section 4.2. The two compositional bistable mechanisms are arranged in parallel to reduce the stage rotation while achieving prescribed translational displacement. The specific geometry parameters of each GLBM used in the mechanism are outlined in Table 5.

#### 6.1. Experimental setup

The assembly of the experimental setup primarily involves four components: the micrometer, force sensor, linear guide, and fabricated prototype, as depicted in Fig. 19(a). To accurately measure the retraction force of the bistable mechanism, we affixed a powerful magnet to the shuttle of the mechanism. This magnet ensures a firm attachment between the shuttle and the probe of the force sensor. Fig. 19(c) illustrates the new bistable mechanism at its second stable position. To

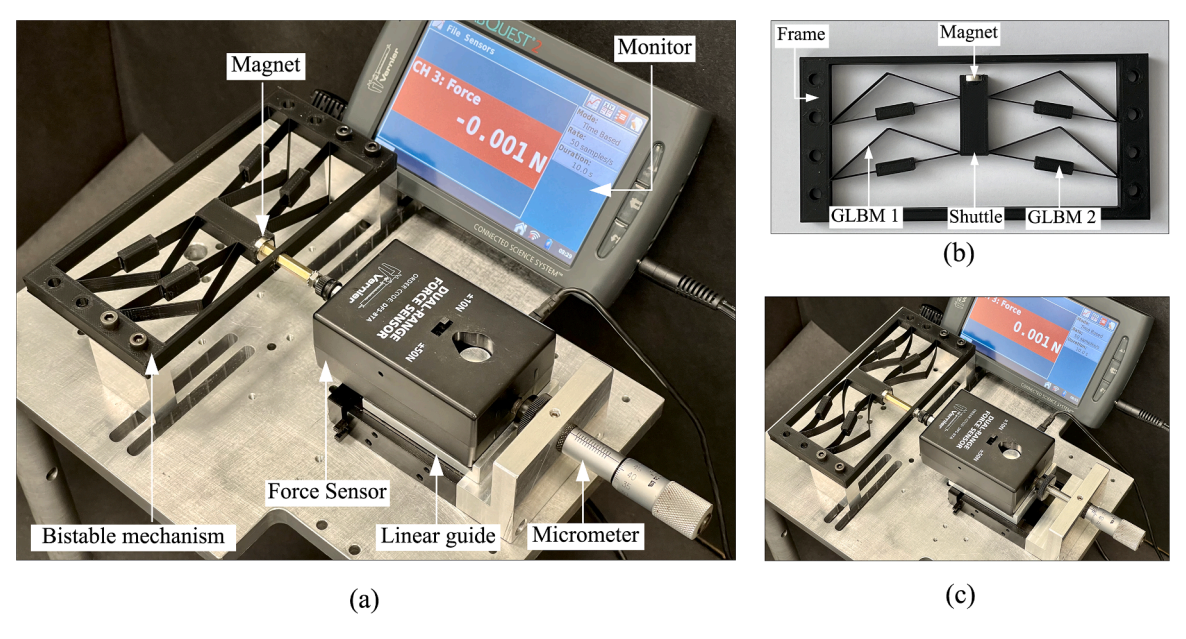


Fig. 19. Experimental setup and the prototype of the bistable mechanism: (a) Experimental setup; (b) 3D-printed prototype; (c) Second stable position of the bistable mechanism.

**Table 5**The geometry parameters of the fabricated bistable mechanism.

GLBM 1	$\alpha_1$ (deg)	$\beta_1$ (deg)	$\gamma_1$ (deg)	$W_1$ (mm)	$L_{11}$ (mm)	$L_{12}$ (mm)	$T_1$ (mm)	$U_1$ (mm)
GLDIII I	-19.17	40.83	10.93	28	32.32	32.32	0.4	8
GLBM 2	$\alpha_2$ (deg)	$\beta_2$ (deg)	$\gamma_2$ (deg)	$W_2$ (mm)	$L_{21}$ (mm)	$L_{22}$ (mm)	$T_2$ (mm)	$U_2$ (mm)
GLDIVI Z	10	10	11.59	36.01	20	20	0.4	8

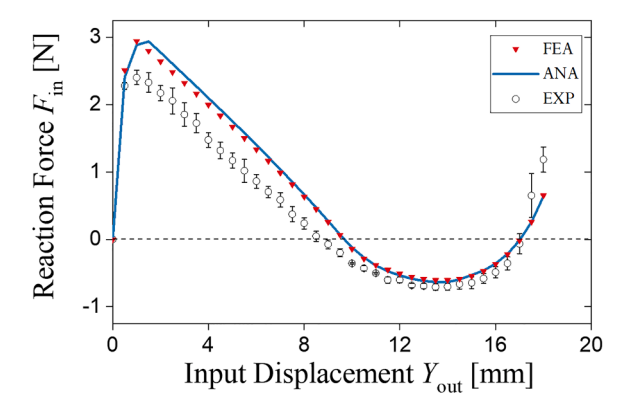


Fig. 20. Force-displacement characteristic of the bistable mechanism.

ensure reliable results, each experimental procedure was repeated three times, and the average of the experiment results was calculated for plot and comparison. Additionally, we calculated the standard deviation of these three results to assess the repeatability of the measurements.

#### 6.2. Experimental results

After conducting the experiment three times, we plotted the average reaction force along with its standard deviation in Fig. 20. A comparison of the experimental results with both the FEA and analytical results revealed a similar pattern. Remarkably, the FEA and analytical results showed better agreement, while the experimental results deviated from both, with a maximum difference of 0.62 N. Several factors could contribute to this deviation, including potential fabrication or assembly errors and undesired elastic deformation of the parts that were assumed to be rigid during the theoretical analysis.

#### 7. Discussions

In this section, we provide a summary of the modeling method and discuss the potential errors associated with this method. This may lead to insights into the approach's applicability and limitations.

## 7.1. Summary of the modeling method

As depicted in Fig. 21, the process of modeling compliant mechanisms using the GLBM entails initializing the geometry property, defining the boundary conditions, formating the force-displacement

relationships, solving the equations, and determining if optimization is required.

The geometry property of a compliant mechanism is initialized by assigning design parameters including the  $L_{i1}$ ,  $L_{i2}$ ,  $\gamma_b$   $\alpha_b$   $\beta_i$  and  $W_i$ . Derivation of the force-displacement relationships of a compliant mechanism using the GLBM generally includes three components, namely the GLBM, force equilibrium, and geometry compatibility. The system equations of the force-displacement relationships can be solved numerically by providing initial guesses in mathematical software, such as Maple. Although the system of equations may appear cumbersome when dealing with complex structures that involve multiple general lumped-compliance beams, the use of the Loop function in Maple or other mathematical software allowed for a streamlined process by eliminating the need for repeating the constitutive equilibrium. This approach significantly reduced the required effort, even for complex structures.

Integrating geometry parameters into the mathematical model of a compliant mechanism enables optimization of its geometry to achieve desired performance characteristics. Designers can vary these parameters to explore the design space and find the optimal geometry that meets the required specifications. For instance, Ref. [14] introduces several novel parameters into the bistable mechanism to better control its behavior. By adjusting the defined geometry parameters, the programmable bistable lattices can be optimized for specific targets such as a larger deformation range or higher stability. However, the optimization in Ref. [14] is done by the enumeration method, which is not efficient. In contrast, the proposed GLBM makes it possible to optimize for multiple objectives simultaneously, which is more efficient and cost-effective.

#### 7.2. Model error

The errors observed could be attributed to model errors and numerical errors. The model error arose from the fact that the constitutive equation relied on the mechanics of the Euler-Bernoulli beam, which disregards the shear effect. In the case of stubby beams, the model error could be significant. To address this issue, the Timoshenko beam theory, which accounts for the effect of shear strains in a beam and adds a correction term to the Euler-Bernoulli beam theory, can be used.

On the other hand, numerical errors could have resulted from the iterative numerical methods used in Maple to solve nonlinear equations. In some cases, these methods may not converge to the exact solution due to issues such as poor initial guesses. Additionally, the mesh quality (element size and shape) in the FEA tool can also contribute to numerical errors. A coarse mesh can lead to significant errors, while a fine mesh

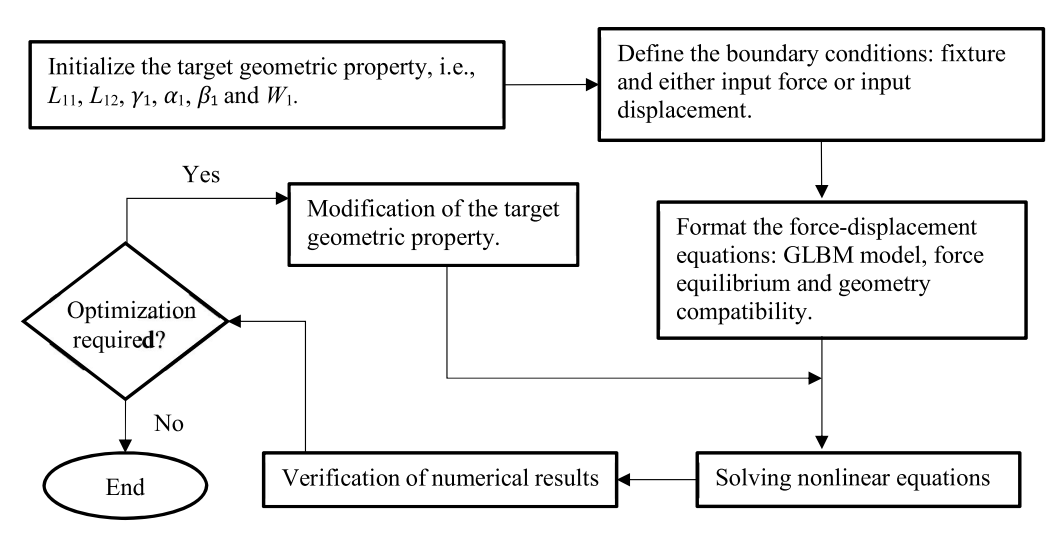


Fig. 21. The general process of using the GLBM to model compliant mechanisms.

can be computationally expensive. However, a finer mesh does not necessarily guarantee better results if the solution does not converge.

#### 8. Conclusion

The paper has proposed an analytical model for a general lumpedcompliance beam, which can accurately and efficiently synthesize force-displacement characteristics in compliant mechanisms that feature any two flexure beams connected in series. The model, termed GLBM, is shown to address the limitations of existing models.

To demonstrate the effectiveness of the proposed GLBM, the present work has conducted thorough analyses on five representative general beam designs and two resulting compliant mechanisms composed of the general beams. The results were compared to nonlinear FEA, where the maximum error between the analytical and FEA models was found to be 6 %. This validation indicates that the GLBM is a promising tool to significantly enhance the design and analysis of compliant mechanisms.

Furthermore, this paper has successfully implemented two experiments to validate the analytical models of the above two compliant mechanisms, the revolute joint and the bistable mechanism. The comparison confirms the credibility of the proposed modeling method.

In our future work, we aim to incorporate the Timoshenko beam theory into our model to capture the shear deformation of the beam cross-sections. This will enable us to better account for the effects of shear strains in our analysis, leading to more accurate results. We believe that this will further enhance the precision of our approach in predicting the behavior of compliant mechanisms with very short

flexure beams. In addition, the GLBM will be utilized in the optimization of the force-displacement performance of compliant mechanisms.

## CRediT authorship contribution statement

**Jiaxiang Zhu:** Data curation, Formal analysis, Funding acquisition, Investigation, Methodology, Software, Validation, Visualization, Writing – original draft, Writing – review & editing. **Guangbo Hao:** Conceptualization, Funding acquisition, Project administration, Resources, Supervision, Writing – review & editing.

#### **Declaration of Competing Interest**

The authors declare that they have no known competing financial interests or personal relationships that could have appeared to influence the work reported in this paper.

#### Data availability

Data will be made available on request.

#### Acknowledgement

Jiaxiang Zhu is grateful for the financial support from the China Scholarship Council (CSC Student ID: 202008300013).

#### Appendix A. Force-displacement characteristic of a flexure beam

As shown in Fig. A1, the loading conditions for a single flexure beam are represented by  $F_{i1}$  (axial force),  $P_{i1}$  (transverse force), and  $M_{i1}$  (moment) acting at the tip of the beam. The resulting displacements are represented by  $X_{i1}$  (displacement along X-axis),  $Y_{i1}$  (displacement along Y-axis), and  $\theta_{i1}$  (rotational angle along Z-axis) with respect to the local coordinate frame. The closed-form solution of the force-displacement characteristic for this flexure beam is represented below [45]:

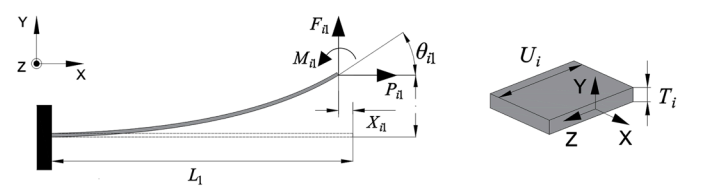


Fig. A1. Simple slender beam with generalized end load.

$$\begin{bmatrix} F_{i1}L_{i1}^{2}/EI \\ M_{i1}L_{i1}^{2}/EI \end{bmatrix} = \begin{bmatrix} 12 & -6 \\ -6 & 4 \end{bmatrix} \begin{bmatrix} Y_{i1}/L_{i1} \\ \theta_{i1} \end{bmatrix} + P_{i1}L_{i1}^{2}/EI \begin{bmatrix} 1.2 & -0.1 \\ -0.1 & 2/15 \end{bmatrix} \begin{bmatrix} Y_{i1}/L_{i1} \\ \theta_{i1} \end{bmatrix}$$

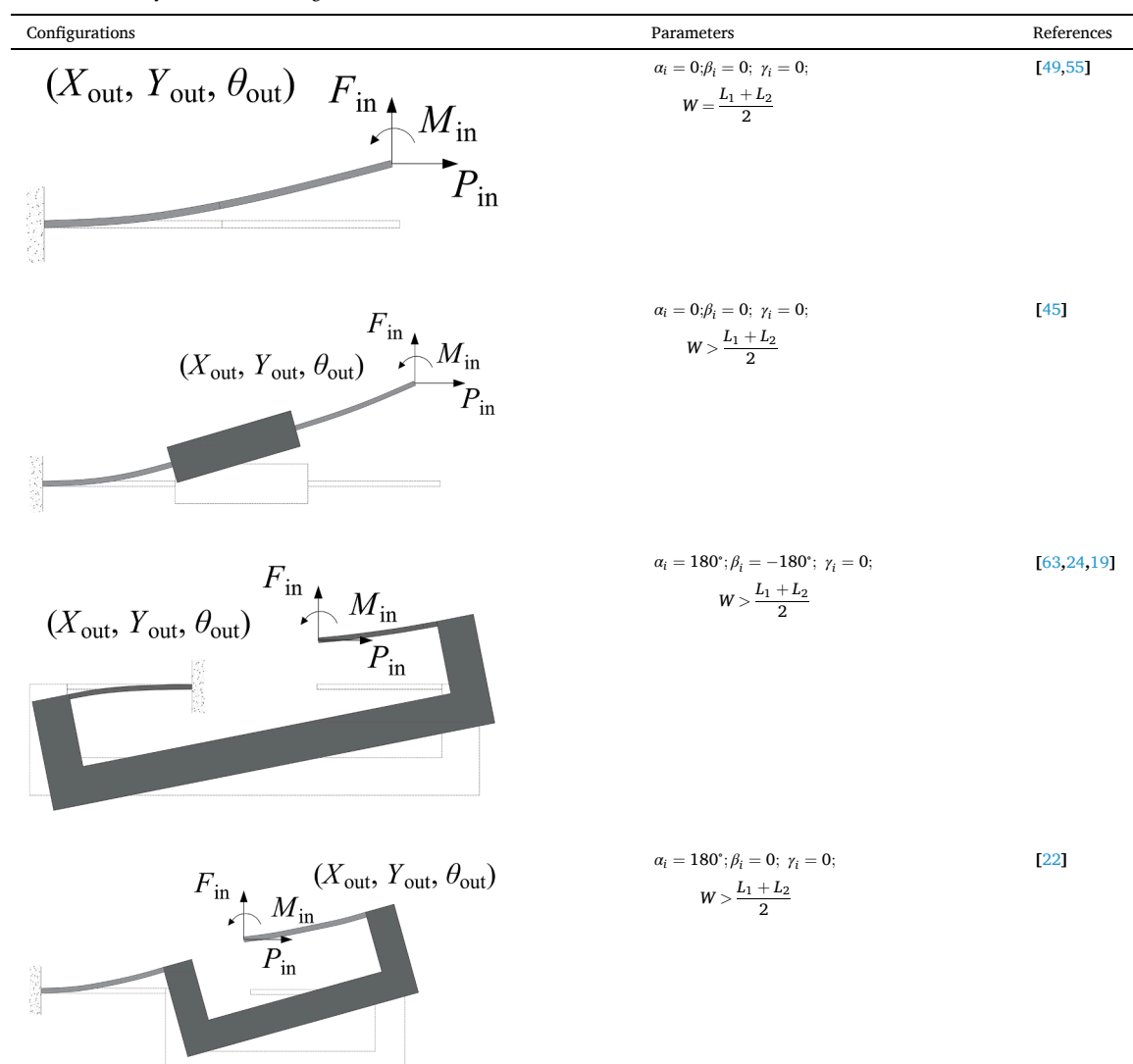
$$\frac{X_{i1}}{L_{i1}} = \left( (T_{i}/L_{i1}^{2})^{2}/12 \right) \cdot \left( P_{i1}L_{i1}^{2}/EI \right) + 0.5[Y_{i1}/L_{i1} \ \theta_{i1}] \begin{bmatrix} 1.2 & -0.1 \\ -0.1 & 2/15 \end{bmatrix} \begin{bmatrix} Y_{i1}/L_{i1} \\ \theta_{i1} \end{bmatrix}$$

$$+ \left( P_{i1}L_{i1}^{2}/EI \right)[Y_{i1}/L_{i1} \ \theta_{i1}] \begin{bmatrix} 1/700 & -1/1400 \\ -1/1400 & 11/6300 \end{bmatrix} \begin{bmatrix} Y_{i1}/L_{i1} \\ \theta_{i1} \end{bmatrix}$$
(A1)

## Appendix B. Summary of commonly-used GLBM configurations

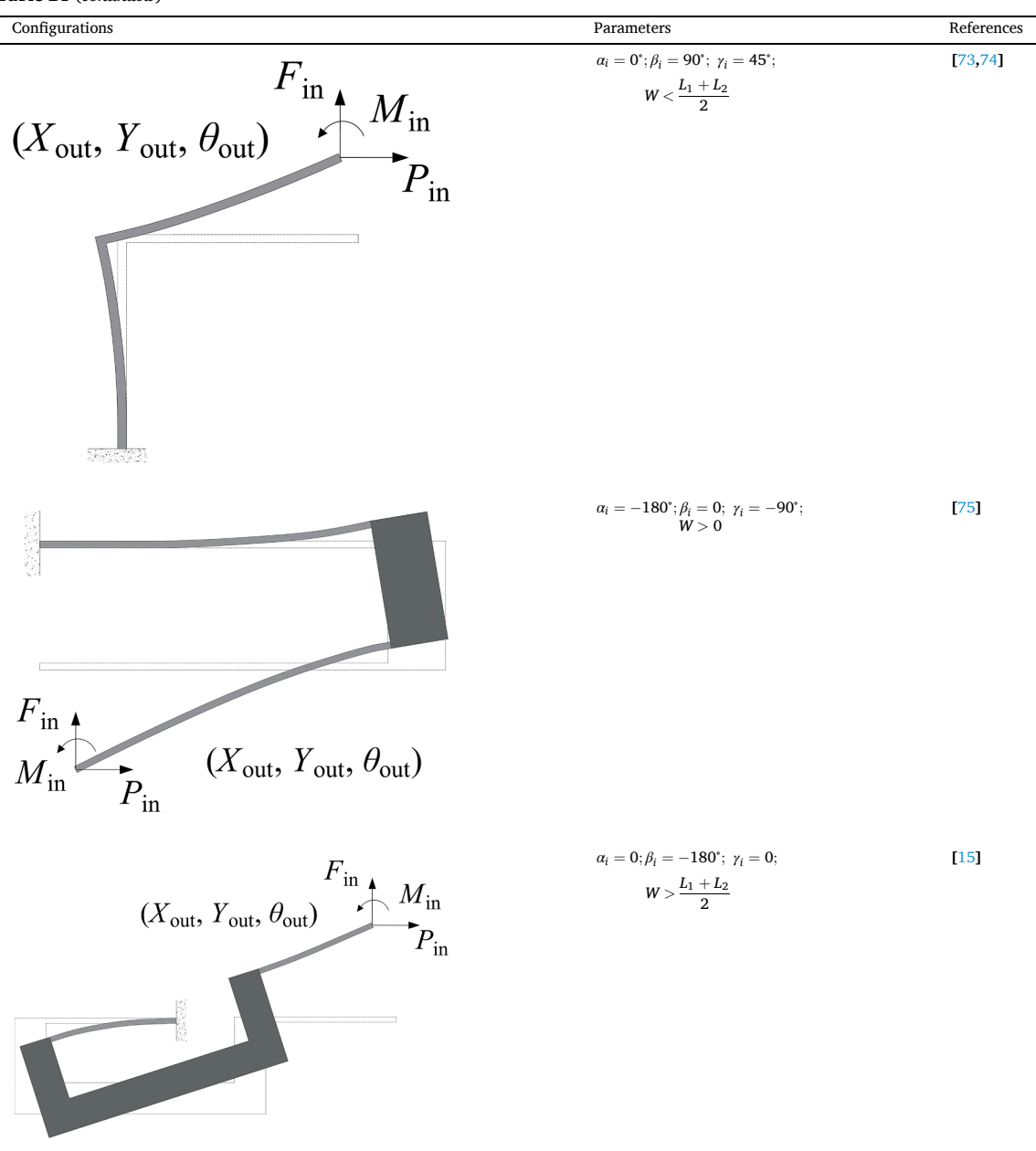
See Appendix Table B1.

Table B1
Several commonly used GLBM configurations



(continued on next page)

Table B1 (continued)



## Appendix C. Abbreviations and Nomenclature

See Appendix Tables C1 and C2

**Table C1**Abbreviations.

FEA	Finite element analysis.
BCM	Beam constraint model
FBD	Free body diagram
GLBM	General lumped compliance beam
PRBM	Pseudo-rigid-body model
CPRBM	Chained- pseudo-rigid-body model
CBCM	Chained beam constraint model
TBCM	Timoshenko beam constraint model
SCM	Smooth curvature model
EIS	Elliptic integral solution
CEIS	Comprehensive elliptic integral solution
MSCM	Multiple smooth curvature model

Table C2
Nomenclature.

$F_i$	Tip force on the flexure beam in the Y-direction
$P_i$	Tip force on the flexure beam in the X-direction
$M_i$	Tip force on the flexure beam about Z-direction
$Y_i$	Tip displacement on the flexure beam in the X-direction
$X_i$	Tip displacement on the flexure beam in the Y-direction
$\Theta_i$	Tip rotation on the flexure beam along Z-direction
$L_i$	The length of ith flexure beam
$L_{i+1}$	The length of $i + 1$ th flexure beam
γi	The $(i + 1)/2$ th angle between ith flexure beam and $i + 1$ th flexure beam with the X-axis
$\alpha_i$	The $(i + 1)/2$ th angle of the <i>i</i> th flexure beam with the <i>X</i> -axis
$\beta_i$	The $(i + 1)/2$ th angle of the $i + 1$ th flexure beam with the <i>X</i> -axis
$F_{si}$	Tip force on the general lumped-compliance beam in the Y-direction
$P_{si}$	Tip force on the general lumped-compliance beam in the X-direction
$M_{si}$	Tip moment on the general lumped-compliance beam about the Z-direction
$Y_{si}$	Tip displacement on the general lumped-compliance beam in the X-direction
$X_{si}$	Tip displacement on the general lumped-compliance beam in the Y-direction
$\theta_{si}$	Tip rotation on the general lumped-compliance beam along Z-direction
I	Moment of inertia of the flexure beam
E	Elastic modulus of the flexure beam

#### References

- Howell LL. Compliant mechanisms. 21st Century kinematics. Springer; 2013.
   p. 189–216. https://doi.org/10.1007/978-1-4471-4510-3 7.
- [2] Hao G, Kong X. A novel large-range XY compliant parallel manipulator with enhanced out-of-plane stiffness. J Mech Des 2012;(6):134. https://doi.org/ 10.1115/1.4006653.
- [3] Tian Y, Ma Y, Wang F, Lu K, Zhang D. A novel XYZ micro/nano positioner with an amplifier based on L-shape levers and half-bridge structure. Sens Actuators A Phys 2020;302:111777. https://doi.org/10.1016/j.sna.2019.111777.
- [4] Lee H-J, Woo S, Park J, Jeong J-H, Kim M, Ryu J, Gweon D-G, Choi Y-M. Compact compliant parallel XY nano-positioning stage with high dynamic performance, small crosstalk, and small yaw motion. Microsyst Technol 2018;24(6):2653–62. https://doi.org/10.1007/s00542-017-3626-z.
- [5] Liang H, Hao G, Olszewski OZ, Pakrashi V. Ultra-low wide bandwidth vibrational energy harvesting using a statically balanced compliant mechanism. Int J Mech Sci 2022:219. https://doi.org/10.1016/j.ijmecsci.2022.107130.
- [6] Blad TWA, van Ostayen RAJ, Herder JL, Tolou N. A statically balanced compliant ortho-planar mechanism for low-frequency energy harvesting. J Mech Des 2022; (7):144. https://doi.org/10.1115/1.4053280.
- [7] Qian F, Xu T-B, Zuo L. Piezoelectric energy harvesting from human walking using a two-stage amplification mechanism. Energy 2019;189. https://doi.org/10.1016/j. energy.2019.116140.
- [8] Deanne CK, Howell LL, Magleby SP. Using compliant mechanisms to improve manufacturability in MEMS. In: ASME 2002 international design engineering technical conferences and computers and information in engineering conference; 2002. p. 247–54. https://doi.org/10.1115/detc2002/dfm-34178.
- [9] Iqbal S, Malik A. A review on MEMS based micro displacement amplification mechanisms. Sens Actuators A Phys 2019;300. https://doi.org/10.1016/j. sna.2019.111666.
- [10] Dorfmeister, M., Kössl, B., Schneider, M., and Schmid, U. 2019. A novel Bi-stable MEMS membrane concept based on a piezoelectric thin film actuator for integrated switching. 10.3390/proceedings2130912.
- [11] Bilancia P, Berselli G. An overview of procedures and tools for designing nonstandard beam-based compliant mechanisms. Comput-Aided Des 2021;134. https://doi.org/10.1016/j.cad.2021.103001.
- [12] Lobontiu N. Compliant mechanisms: design of flexure hinges. CRC press; 2002. https://doi.org/10.1201/9781420040272.
- [13] Tran NDK, Wang D-A. Design of a crab-like bistable mechanism for nearly equal switching forces in forward and backward directions. Mech Mach Theory 2017; 115:114–29. https://doi.org/10.1016/j.mechmachtheory.2017.05.005.
- [14] Liu T, Hao G. Design of deployable structures by using bistable compliant mechanisms. Micromachines (Basel) 2022;(5):13. https://doi.org/10.3390/ mi13050651.
- [15] Han Q, Jin K, Chen G, Shao X. A novel fully compliant tensural-compresural bistable mechanism. Sens Actuators A Phys 2017;268:72–82. https://doi.org/ 10.1016/j.sna.2017.10.012.
- [16] Chen G, Zhang S. Fully-compliant statically-balanced mechanisms without prestressing assembly: concepts and case studies. Mech Sci 2011;2(2):169–74. https://doi.org/10.5194/ms-2-169-2011.
- [17] Pan B, Zhao H, Zhao C, Zhang P, Hu H. Nonlinear characteristics of compliant bridge-type displacement amplification mechanisms. Precis Eng 2019;60:246–56. https://doi.org/10.1016/j.precisioneng.2019.08.012.
- [18] Ma H-W, Yao S-M, Wang L-Q, Zhong Z. Analysis of the displacement amplification ratio of bridge-type flexure hinge. Sens Actuators A Phys 2006;132(2):730–6. https://doi.org/10.1016/j.sna.2005.12.028.

- [19] Kong K, Chen G, Hao G. Kinetostatic modeling and optimization of a novel horizontal-displacement compliant mechanism. J Mech Robot 2019;(6):11. https://doi.org/10.1115/1.4044334.
- [20] Hao G, Li H, He X, Kong X. Conceptual design of compliant translational joints for high-precision applications. Front Mech Eng 2014;9(4):331–43. https://doi.org/ 10.1007/s11465-014-0321-y.
- [21] Li S, Hao G, Chen Y, Zhu J, Berselli G. Nonlinear analysis of a class of inversion-based compliant cross-spring pivots. J Mech Robot 2021:1–29. https://doi.org/10.1115/1.4052514.
- [22] Hao, G., Yu, J., and Liu, Y. 2018. Compliance synthesis of a class of planar compliant parallelogram mechanisms using the position space concept. 10.1109 /remar.2018.8449882.
- [23] Chen G, Han Q, Jin K. A fully compliant tristable mechanism employing both tensural and compresural segments. J Mech Robot 2019;12(1). https://doi.org/ 10.1115/1.4044736.
- [24] Wu K, Hao G. Design and nonlinear modeling of a novel planar compliant parallelogram mechanism with general tensural-compresural beams. Mech Mach Theory 2020;152. https://doi.org/10.1016/j.mechmachtheory.2020.103950.
- [25] Henning S, Zentner L. Analysis of planar compliant mechanisms based on nonlinear analytical modeling including shear and lateral contraction. Mech Mach Theory 2021;164. https://doi.org/10.1016/j.mechmachtheory.2021.104397.
- [26] Odhner LU, Dollar AM. The smooth curvature model: an efficient representation of Euler–Bernoulli flexures as robot joints. IEEE Trans Rob 2012;28(4):761–72. https://doi.org/10.1109/TRO.2012.2193232.
- [27] Chen G, Ma F, Hao G, Zhu W. Modeling large deflections of initially curved beams in compliant mechanisms using chained beam constraint model. J Mech Robot 2019;11(1). https://doi.org/10.1115/1.4041585.
- [28] Chen G, Ma F. Kinetostatic modeling of fully compliant bistable mechanisms using Timoshenko beam constraint model. J Mech Des 2015;137(2). https://doi.org/ 10.1115/1.4029024.
- [29] Li R, Yang Z. Modeling the nonlinear deflection of elliptical-arc-fillet leaf springs. Mech Mach Theory 2022;176. https://doi.org/10.1016/j. mechmachtheory.2022.105037.
- [30] Li R, Yang Z, Chen G, Wu B. Analytical solutions for nonlinear deflections of corner-fillet leaf-springs. Mech Mach Theory 2021;157. https://doi.org/10.1016/j. mechmachtheory.2020.104182.
- [31] Sen S, Awtar S. Nonlinear strain energy formulation of a generalized bisymmetric spatial beam for flexure mechanism analysis. J Mech Des N Y 2014;136(2): 0210021–2100213. https://doi.org/10.1115/1.4025705.
- [32] Yu Y-Q, Zhang N. Dynamic modeling and performance of compliant mechanisms with inflection beams. Mech Mach Theory 2019;134:455–75. https://doi.org/ 10.1016/j.mechmachtheory.2019.01.010.
- [33] Jin M, Zhu B, Mo J, Yang Z, Zhang X, Howell LL. A CPRBM-based method for large-deflection analysis of contact-aided compliant mechanisms considering beam-to-beam contacts. Mech Mach Theory 2020;145. https://doi.org/10.1016/j.mechmachtheory.2019.103700.
- [34] Yu Y-Q, Feng Z-L, Xu Q-P. A pseudo-rigid-body 2R model of flexural beam in compliant mechanisms. Mech Mach Theory 2012;55:18–33. https://doi.org/ 10.1016/j.mechmachtheory.2012.04.005.
- [35] Su H-J. A pseudorigid-body 3R model for determining large deflection of cantilever beams subject to tip loads. J Mech Robot 2009;1(2). https://doi.org/10.1115/ 1.3046148
- [36] Yu Y-Q, Li Q, Xu Q-P. Pseudo-rigid-body dynamic modeling and analysis of compliant mechanisms. Proc Inst Mech Eng Part C J Mech Eng Sci 2017;232(9): 1665–78. https://doi.org/10.1177/0954406217707547.
- [37] Zhang A, Chen G. A comprehensive elliptic integral solution to the large deflection problems of thin beams in compliant mechanisms. J Mech Robot 2013;5(2). https://doi.org/10.1115/1.4023558.

- [38] Iwatsuki N, Kosaki T. Large deformation analysis and synthesis of elastic closed-loop mechanism made of a certain spring wire described by free curves. Chin J Mech Eng 2015;28(4):756–62. https://doi.org/10.3901/cjme.2015.0506.067.
- [39] Howell LL, Midha A. Parametric deflection approximations for end-loaded, large-deflection beams in compliant mechanisms. J Mech Des 1995;117(1):156–65. https://doi.org/10.1115/1.2826101.
- [40] Howell LL, Midha A, Norton TW. Evaluation of equivalent spring stiffness for use in a pseudo-rigid-body model of large-deflection compliant mechanisms. J Mech Des 1996;118(1):126–31. https://doi.org/10.1115/1.2826843.
- [41] Chen G, Xiong B, Huang X. Finding the optimal characteristic parameters for 3R pseudo-rigid-body model using an improved particle swarm optimizer. Precis Eng 2011;35(3):505–11. https://doi.org/10.1016/j.precisioneng.2011.02.006.
- [42] Yu Y-Q, Zhu S-K. 5R pseudo-rigid-body model for inflection beams in compliant mechanisms. Mech Mach Theory 2017;116:501–12. https://doi.org/10.1016/j. mechmachtheory.2017.06.016.
- [43] Pauly J, Midha A. Pseudo-rigid-body model chain algorithm: Part 2 Equivalent representations for combined load boundary conditions. In: ASME 2006 International design engineering technical conferences and computers and information in engineering conference; 2006. p. 183–90. 10.1115/detc2 006-99463.
- [44] Pauly J, Midha A. Pseudo-rigid-body model chain algorithm: Part 1 Introduction and concept development. In: ASME 2006 International design engineering technical conferences and computers and information in engineering conference; 2006. p. 173–81. 10.1115/detc2006-99460.
- [45] Awtar S, Sen S. A generalized constraint model for two-dimensional beam flexures: nonlinear load-displacement formulation. J Mech Des 2010;132(8):081008. https://doi.org/10.1115/1.4002005.
- [46] Hao G, Kong X. A normalization-based approach to the mobility analysis of spatial compliant multi-beam modules. Mech Mach Theory 2013;59:1–19. https://doi. org/10.1016/j.mechmachtheory.2012.08.013.
- [47] Sen S, Awtar S. A closed-form nonlinear model for the constraint characteristics of symmetric spatial beams. J Mech Des 2013;(3):135. https://doi.org/10.1115/ 1.4023157
- [48] Radgolchin M, Moeenfard H. A constraint model for beam flexure modules with an intermediate semi-rigid element. Int J Mech Sci 2017;122:167–83. 10.1016/j. iimecsci.2016.10.011.
- [49] Ma F, Chen G. Bi-BCM: a closed-form solution for fixed-guided beams in compliant mechanisms. J Mech Robot 2017;9(1). https://doi.org/10.1115/1.4035084.
- [50] Bilancia P, Baggetta M, Hao G, Berselli G. A variable section beams based Bi-BCM formulation for the kinetostatic analysis of cross-axis flexural pivots. Int J Mech Sci 2021;205. https://doi.org/10.1016/j.ijmecsci.2021.106587.
   [51] Howell LL, Leonard JN. Optimal loading conditions for non-linear deflections. Int J
- [51] Howell LL, Leonard JN. Optimal loading conditions for non-linear deflections. Int J Non Linear Mech 1997;32(3):505–14. https://doi.org/10.1016/S0020-7462(96) 00069-8.
- [52] Cammarata A, Lacagnina M, Sequenzia G. Alternative elliptic integral solution to the beam deflection equations for the design of compliant mechanisms. Int J Interact Des Manuf (IJIDeM) 2018;13(2):499–505. https://doi.org/10.1007/ s12008-018-0512-6.
- [53] Lyon SM, Howell LL, Roach GM. Modeling flexible segments with force and moment end loads via the pseudo-rigid-body model. In: ASME 2000 International mechanical engineering congress and exposition; 2000. p. 883–90. https://doi.org/ 10.1115/imece2000-2390.
- [54] Kimball C, Tsai L-W. Modeling of flexural beams subjected to arbitrary end loads. J Mech Des 2002;124(2):223–35. https://doi.org/10.1115/1.1455031.
- [55] Ma F, Chen G. Modeling large planar deflections of flexible beams in compliant mechanisms using chained beam-constraint-model1. J Mech Robot 2016;8(2). https://doi.org/10.1115/1.4031028.

- [56] Kontoudis GP, Liarokapis M, Vamvoudakis KG, Furukawa T. An adaptive actuation mechanism for anthropomorphic robot hands. Front Robot AI 2019;6:47. https://doi.org/10.3389/frobt.2019.00047.
- [57] Kuresangsai P, Cole MOT, Hao G. Grasp stability and design analysis of a flexurejointed gripper mechanism via efficient energy-based modeling. IEEE Rob Autom Lett 2022:1–8. https://doi.org/10.1109/lra.2022.3220152.
- [58] Liarokapis MV, Dollar AM. Post-contact, in-hand object motion compensation with adaptive hands. IEEE Trans Autom Sci Eng 2016;15(2):456–67.
- [59] Awtar S, Slocum AH, Sevincer E. Characteristics of beam-based flexure modules. J Mech Des 2007;129(6):625–39. https://doi.org/10.1115/1.2717231.
- [60] Awtar S. Synthesis and analysis of parallel kinematic XY flexure mechanisms. Cambridge, MA: Massachusetts Institute of Technology; 2003.
- [61] Hartog Den, P J. Advanced strength of materials. Courier Corporation; 1987.
- [62] Archer, R.R., Crandall, S.H., Dahl, N.C., and Lardner, T.J.J., 1959, An introduction to the mechanics of solids.
- [63] Masters ND, Howell LL. A self-retracting fully compliant bistable micromechanism. J Microelectromech Syst 2003;12(3):273–80. https://doi.org/10.1109/ imems 2003.811751
- [64] Luharuka R, Hesketh PJ. Design of fully compliant, in-plane rotary, bistable micromechanisms for MEMS applications. Sens Actuators A Phys 2007;134(1): 231–8. https://doi.org/10.1016/j.sna.2006.04.030.
- [65] Han Q, Huang X, Shao X. Nonlinear kinetostatic modeling of double-tensural fully-compliant bistable mechanisms. Int J Non Linear Mech 2017;93:41–6. https://doi.org/10.1016/j.ijnonlinmec.2017.04.020.
- [66] Chen G, Wu H, Li B, Wang MY. Fully compliant bistable mechanisms with enhanced pitch stiffness. Mech Syst Signal Process 2021;161. https://doi.org/ 10.1016/j.ymssp.2021.107926.
- [67] Dunning AG, Tolou N, Pluimers PP, Kluit LF, Herder JL. Bistable compliant mechanisms: corrected finite element modeling for stiffness tuning and preloading incorporation. J Mech Des 2012;(8):134. https://doi.org/10.1115/1.4006961.
- [68] Hao G, He X, Awtar S. Design and analytical model of a compact flexure mechanism for translational motion. Mech Mach Theory 2019;142. https://doi. org/10.1016/j.mechmachtheory.2019.103593.
- [69] Rommers J, van der Wijk V, Herder JL. A new type of spherical flexure joint based on tetrahedron elements. Precis Eng 2021;71:130–40. https://doi.org/10.1016/j. precisioneng.2021.03.002.
- [70] Naves M, Brouwer DM, Aarts RGKM. Building block-based spatial topology synthesis method for large-stroke flexure hinges. J Mech Robot 2017;9(4). https://doi.org/10.1115/1.4036223.
- [71] Hao G, Yu J, Liu Y. Compliance synthesis of a class of planar compliant parallelogram mechanisms using the position space concept. In: 2018 International conference on reconfigurable mechanisms and robots (ReMAR); 2018. p. 1–10.
- [72] Rommers J, Naves M, Brouwer DM, Herder JL. A flexure-based linear guide with torsion reinforcement structures. J Mech Robot 2021;14(3). https://doi.org/ 10.1115/1.4052971.
- [73] Naves M, Aarts RGKM, Brouwer DM. Large stroke high off-axis stiffness three degree of freedom spherical flexure joint. Precis Eng 2019;56:422–31. https://doi. org/10.1016/j.precisioneng.2019.01.011.
- [74] Rommers J, Herder J. Design of a folded leaf spring with high support stiffness at large displacements using the inverse finite element method. In: Advances in mechanism and machine science: proceedings of the 15th IFToMM world congress on mechanism and machine science. 15; 2019. p. 2109–18.
- [75] Zhang Z, Liu Z, Yan P. Design of a flexure-based XY positioning stage with balanced axial forces on decoupling modules. In: 2016 IEEE International conference on manipulation, manufacturing and measurement on the nanoscale (3M-NANO); 2016. p. 83–8.

# <u>Update</u>

# **International Journal of Mechanical Sciences**

Volume 272, Issue , 15 June 2024, Page

DOI: https://doi.org/10.1016/j.ijmecsci.2024.109169

FISEVIER

Contents lists available at ScienceDirect

## International Journal of Mechanical Sciences

journal homepage: www.elsevier.com/locate/ijmecsci



## Corrigendum



Corrigendum to "Modelling of a general lumped-compliance beam for compliant mechanisms" [International Journal of Mechanical Sciences, Volume 263, 108779]

Jiaxiang Zhu, Guangbo Hao

School of Engineering and Architecture-Electrical and Electronic Engineering, University College Cork, Cork, Ireland

Following the publication of our article, we have identified errors in the representation of two figures that require correction. The inaccuracies are detailed below.

1. Fig. 1: Configuration of a general beam: (a) geometry parameters of the GLBM; (b) FBD of the general beam

There was error on the labelling of parameter  $\gamma_i$  in Fig. 1(a) in the original article. The corrected figure is provided below.

2. Fig. 14: Bistable mechanism with increased out-of-plane stiffness: (a) geometry parameters; (b) deformed configuration and the FBD of the shuttle.

The original labelling of Fig. 14(a) is missing parameter  $\gamma_2$ . The corrected version is provided below.

The authors extend their sincere apologies for any inconvenience caused by these oversights.

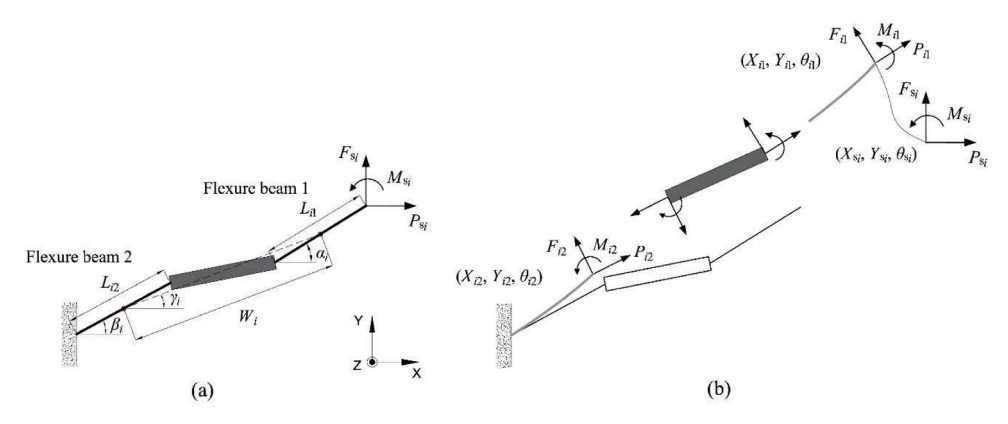


Fig. 1. Configuration of a general beam: (a) geometry parameters of the GLBM; (b) FBD of the general beam.

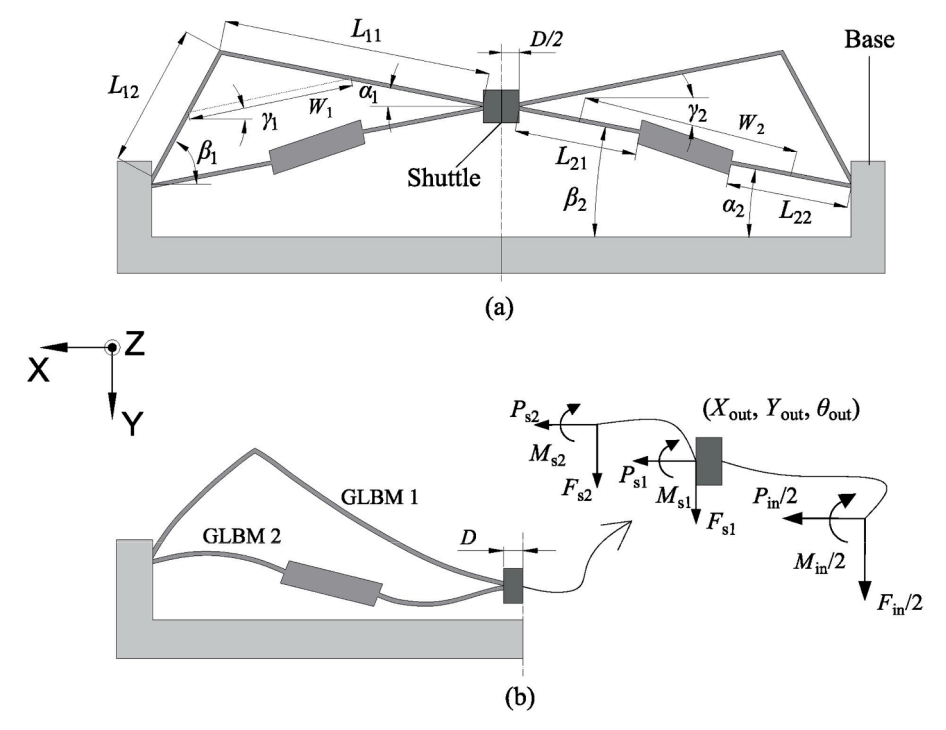


Fig. 14. Bistable mechanism with increased out-of-plane stiffness: (a) geometry parameters; (b) deformed configuration and the FBD of the shuttle.